Mechanical Systems and Signal Processing 208 (2024) 110916

Contents lists available at ScienceDirect

Mechanical Systems and Signal Processing

journal homepage: www.elsevier.com/locate/ymssp

Spectral estimation model for linear displacement and vibration monitoring with GBSAR system

Benyamin Hosseiny [a], Jalal Amini [a,*], Hossein Aghababaei [b]

[a] School of Surveying and Geospatial Engineering, College of Engineering, University of Tehran, Tehran, Iran
[b] Department of Earth Observation Science (EOS), Faculty of Geo-Information Science and Earth Observation (ITC), University of Twente, 7514 AE Enschede, the Netherlands

ARTICLE INFO

Communicated by: Javad Baqersad

Keywords:
Deformation monitoring
Multiple Input Multiple Output (MIMO) radar
SAR interferometry
Beamforming
Capon
MUSIC
CLEAN

ABSTRACT

In recent years, there has been a growing interest in the development of ground-based Synthetic Aperture Radars (GBSAR) for the purpose of monitoring structural displacements. GBSAR offers high-resolution monitoring over a wide area and can capture data every few minutes. However, compact high-frequency multiple input multiple output (MIMO) radars have emerged as an alternative for monitoring sub-second displacements, such as structural vibrations. MIMO radar has sub-second acquisition interval. However, it has limited cross-range resolution compared to GBSAR, and interference between antennas and presence of multiple scatterers in the scene can cause strong sidelobes in the processed data. On the other hand, GBSAR utilizes a long synthetic aperture to achieve high cross-range resolution. However, due to its longer data acquisition time compared to MIMO radar, conventional methods are insufficient for detecting scatterers' sub-second displacements that occur during the data acquisition process. This study proposes a method to effectively monitor sub-second or sub-minute displacements using GBSAR signals. The proposed method enhances the conventional radar interferometric processes by employing spectral estimation, allowing for multi-dimensional detection of targets' azimuth angle, linear displacement, and vibrational characteristics. Consequently, this method improves both the processing of MIMO radar data and enables high-resolution fast displacement monitoring from GBSAR signals. The paper presents the theoretical details and mathematical formulations of the proposed method for both MIMO radar and GBSAR imaging modes. To evaluate the effectiveness of the proposed method, numerical simulations and real experiments are conducted. The experimental results validate the capability of the proposed method in both GBSAR and MIMO configuration modes for high-resolution monitoring of fast linear displacements and vibrations. The results exhibit promising signal-to-noise ratio (SNR) and peak-to-sidelobe ratio (PSLR) values.

1. Introduction

Radar interferometry has been investigated, experimented and adapted in a wide range of applications in radar remote sensing. The space-based technique makes it feasible to monitor targets' displacement with up to sub-millimeter accuracy [1–3]. Multi-baseline and/or time-series Synthetic aperture radar (SAR) provides cross-range resolution with interferometric processing of radar signals

* Corresponding author.
E-mail address: jamini@ut.ac.ir (J. Amini).

https://doi.org/10.1016/j.ymssp.2023.110916
Received 9 March 2023; Received in revised form 14 October 2023; Accepted 2 November 2023
Available online 30 November 2023
0888-3270/© 2023 Published by Elsevier Ltd.

acquired at different cross-range locations [4]. Radar interferometry is thus the basis for multi-dimensional radar imaging and displacement monitoring. While the satellite based SAR interferometry (InSAR) is a mature tool for large-scale monitoring of Earth environment, the terrestrial (or ground-based) radar interferometry (TRI), ground-based SAR (GBSAR) interferometry (GBInSAR), and recently ground-based multiple input multiple output (MIMO) radars are mainly categorized as noncontact systems for monitoring dynamics of small areas with a better temporal resolution and lower atmospheric impact than satellite data [5–7].

GBSAR systems generally enable cross-range resolution by moving the radar sensor on a mechanical rail in a specified trajectory [8]. MIMO systems, as a well-known ground based data collection, can improve the data acquisition interval to a fraction of a second in the cost of using an extra number of physical antennas [9,10]. In this context, MELISSA [11] was the first ground-based MIMO system, comprising twelve transmitter and twelve receiver antennas, developed for geophysical and structural displacement monitoring [12]. Recent studies have also demonstrated the effectiveness of automotive 77 GHz W-band MIMO radars for structural monitoring [13–15]. In fact, higher operational frequency results in a more compact and lighter system and, as a result, simpler deployment [9]. These systems are suitable for monitoring a single object such as a building, bridge, or wind turbine [16–18]. In practice, however, several issues such as signal interferences, high sidelobes, and signal-to-noise ratio (SNR) have to be addressed in order to obtain accurate results in terms of target focusing and displacement estimation from GBSAR or MIMO radar data.

Spectral estimation (SE) techniques have shown great potential in processing SAR data in order to detect signals of interest [17,19,20]. In general, SE aims to estimate the signal's power spectrum. Fourier transform (FT) is the simplest but most prevalent SE technique. These methods have yielded intriguing results in estimating parameters of interest from observed signals, even when the SNR is low [19,21]. In recent years, SE methods have been developed to resolve multi-dimensional SAR problems. Compared to the conventional displacement mapping using time-series SAR data and based upon Persistent Scatterer Interferometric (PSI) technique, which only process the phase information and disregard signal's amplitude [21–24], SE methods make use of the complete information of SAR data (phase and amplitude) of a stack of radar or SAR signals to separate multiple scattering targets' positions and displacement characteristics [25]. In particular, SE techniques have been used extensively in SAR tomography (TomoSAR) to retrieve the 3D-reflectivity of natural or urban targets, such as urban height reconstruction [26], or volumetric targets, such as forest biomass [27] and ice thickness [28] using multi-baseline SAR data. SE methods have also shown great potential in multi-dimensional monitoring of urban areas, such as 4D and 5D differential TomoSAR reconstruction of structures' linear displacement velocity and thermal dilation [21,29,30].

Real aperture radar (RAR) can provide a high data acquisition frequency in the kilohertz range. Consequently, recent studies have demonstrated the performance of RARs as contactless systems for monitoring fast displacements or vibrations [31,32]. In contrast to RAR, one of the major challenges in GBSAR imaging is the relatively long data acquisition interval, often spanning several minutes. This limitation hinders its application for real-time and fast displacement monitoring, such as monitoring structural vibrations [33]. Additionally, mechanical fluctuations during the movement of the radar in GBSAR imaging can potentially impact the desired consistent azimuth sampling. This can introduce noise into the collected data, further complicating the imaging process [34]. Even though these issues are significantly resolved by MIMO technology, this imaging mode requires a large number of physical antennas to achieve cross-range resolution that is comparable to GBSAR. This requirement leads to a significant increase in system size and cost. Additionally, the resulting data may include strong sidelobes due to antenna interferences and the presence of multiple scatterers within one bin, further adding complexity to the imaging process [35]. This paper presents a monitoring system that utilizes signals collected from ground-based radar and SE methods to achieve high-resolution results. The main focus of the paper is to develop a model that can estimate both linear and nonlinear displacements of scattering targets while acquiring data through radar signals. The proposed model utilizes various spectral estimation techniques and takes into account data acquired from both GBSAR and MIMO radar configuration modes. The model encompasses the detection of linear displacement velocity, amplitude, and frequency of nonlinear vibrational displacement, as well as the azimuth location of the detected targets. By employing this framework, the system offers multi-dimensional imaging capability while suppressing sidelobes and achieving high signal-to-noise ratio (SNR). Furthermore, it addresses a key limitation of GBSAR systems by enabling the detection of fast and real-time displacements during data acquisition.

Finally, the main contributions of this paper are summarized as follows:

- Proposing a linear and vibrational displacement monitoring model based upon GBSAR imaging and spectral estimation method: this method improves the spatial localization of the detected deforming areas on the monitored object
- Proposing a linear and vibrational displacement monitoring model based upon ground-based MIMO radar imaging and spectral estimation method: this method increases the focused signals' SNR, and hence, improves the results' robustness
- Evaluating the proposed frameworks by simulated and real experiments
- Various analyses on the performance evaluation of the proposed frameworks on MIMO radar and SAR imaging modes.

The rest of the paper is organized as follows: Section 2 presents the proposed methodology including the regarding theoretical background. The results of the simulations and experiments are brought in Section 3. Finally, the summary of this study and concluding marks are drawn in Section 4.

2. Methodology

In this section, the paper introduces a SAR imaging and processing model designed specifically for near real-time monitoring of sub-second scale fast displacements. The focus is on presenting innovative data acquisition modes and processing algorithms that enable precise estimation of various target parameters from radar signals. The proposed model aims to accurately estimate the linear

displacement velocity and vibration characteristics of targets, while also determining their angle of arrival (AoA).

2.1 System description and data acquisition modes

The proposed method is demonstrated using two radar imaging modes: low-resolution MIMO radar and high-resolution GBSAR. MIMO radar utilizes multiple transmitter and receiver antennas to achieve range and AoA discrimination, allowing for sub-second data acquisition intervals. On the other hand, GBSAR synthesizes a large aperture by moving along a predetermined trajectory on a mechanical rail of significant length. Fig. 1 provides a schematic comparison of signal transmission and virtual antenna generation between MIMO radar and GBSAR modes. The subsequent subsections will provide a detailed explanation of each imaging mode.

2.1.1 MIMO radar acquisition mode

In the MIMO radar configuration, the arrangement of multiple transmitter and receiver antennas allows for cross-range resolution and synthesis of a large aperture. This means that instead of physically moving the sensor along a trajectory, the fixed antennas can effectively monitor phenomena with a sub-second data acquisition interval. This approach enables accurate and precise monitoring of various phenomena without the need for physical movement [36]. Compared to the conventional phased arrays, the main feature of the MIMO array is that the antenna arrangement is not required to be uniform. Thus, as a popular antenna arrangement geometry, it is possible to attain $N_{Rx} \times N_{Tx}$ virtual antennas from $N_{Rx} + N_{Tx}$ antenna elements when the combination of N_{Tx} transmitter antennas (Tx) with non-Nyquist $N_{Rx}\lambda/2$ spacing and N_{Rx} receiver antennas (Rx) with $\lambda/2$ is employed, where λ is the radar signal's wavelength [36,37]. Fig. 1-a shows the signal transmission geometry by linear MIMO radar's virtual transmitter and receiver antennas. In this case, one virtual transmitter sends signal and then the virtual receivers simultaneously collect the echo waves.

In this study, a multi-temporal stack of range–azimuth MIMO radar signals with zero spatial baseline is chosen as the appropriate data acquisition mode for their proposed algorithms. In this mode, the raw acquired data would form a 3D matrix with dimensions $N_r \times N_a \times N_q$. Here, N_r, N_a, and N_q are the number of samples in directions of radar's line-of-sight (LOS) or range denoted as r, azimuth denoted as a, and repeat time (or time) denoted as q, respectively (Fig. 1-b). Thus, the collected raw cube data can be represented and modeled using this matrix structure as follows[36,37]:

$$s_{if}(t,m,q) = \exp\left\{ j2\pi \left(f_0\tau(z) + k_r\tau(q)t - \frac{k\tau^2(q)}{2} + \frac{\ell_m \sin\theta}{\lambda} \right) \right\} \tag{1}$$

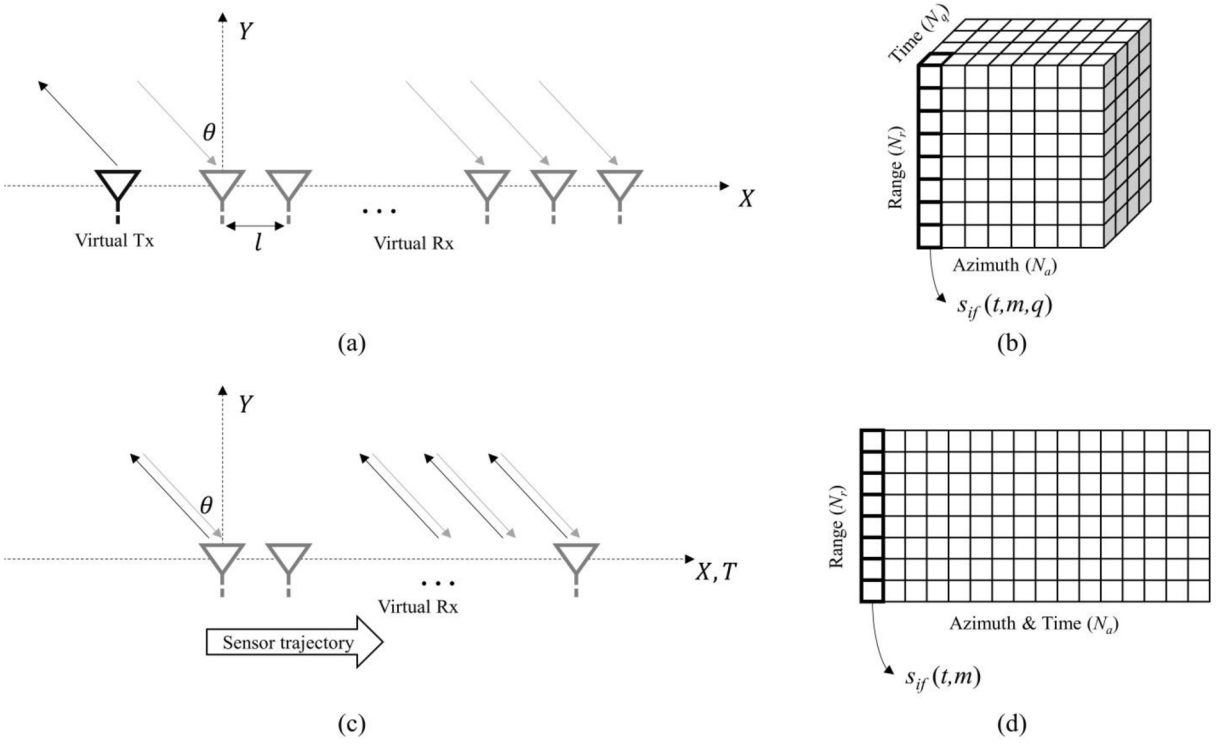

Fig. 1. Schematic diagram of data acquisition modes: (a) MIMO radar antenna and signal transmission configuration. (b) MIMO radar collected data array during the acquisition time. (c) GBSAR antenna and signal transmission configuration. (d) GBSAR collected data array during the acquisition time.

where $s_{if}(t, m, q)$ is the received raw intermediate frequency signal by the MIMO radar, f_0, and k, are the operating signal's starting frequency, chirp slope, respectively, $\tau = (R_1 + R_2)/c$ represents the signal's two-way propagation delay related to the scattering target's range to the transmitter (R_1) and receiver (R_2) antennas, θ is the scattering target's cross-range angle or AoA, and ℓ_m is the radar's m^{th} virtual antenna location on the azimuth or along-track axis for $\ell_m = ml$, where l is the distance between two adjacent MIMO virtual arrays, and $m = 0, 1, \ldots, N_a - 1$.

2.1.2 GBSAR acquisition mode

Conventional monostatic radar systems typically cannot estimate angles of arrival (AoA) without collecting signals from different viewing angles. However, a GBSAR system can overcome this limitation by moving a radar sensor along a mechanical rail. In Fig. 1-c, the signal transmission geometry of a linear GBSAR is depicted. At each step along its trajectory, the sensor transmits signals and collects the resulting echo waves separately. By providing a synthetic aperture that is often longer than MIMO radars, the GBSAR system offers high-resolution cross-range discrimination.

However, extracting sub-second displacements, such as structural vibrations, from GBSAR data poses significant challenges due to the radar sensor's movement and the longer data acquisition interval (usually longer than a few minutes). In our previous work [33], a continuous monitoring algorithm was demonstrated, enabling the monitoring of fast displacements using GBSAR data. However, the algorithm's performance and accuracy decrease in scenarios with a high number of targets exhibiting different azimuth locations or displacement behavior within the same range bin, or when the targets' backscattering power is weak. Furthermore, the presence of a displacing target during SAR imaging can result in blurred images with undesired artifacts and low SNR. To address these challenges, the proposed workflow aims to decompose and mitigate the effects of scatterers' displacements from the received signal. The details of this workflow will be described in the next section.

In this study, a collection of radar signals acquired during the radar's movement on its specified trajectory in a GBSAR system is chosen as a proper data acquisition mode for fast detection of linear and vibrational displacements from the proposed algorithms. In this case, we can formulate the recorded GBSAR signals as a multi-temporal stack of N_a one-dimensional range profiles with a spatial baseline from the sensor's zero location along the azimuth axis. Therefore, the raw acquired GBSAR data would form a 2D $N_r \times N_a$ matrix, where N_r, and N_a are the number of samples in range, azimuth directions (Fig. 1-d). In the case of monostatic GBSAR, the received raw signal can be modeled as follows:

$$s_{if}(t, m) = \exp\left\{ j2\pi \left(f_0\tau + k_r\tau t - \frac{k\tau^2}{2} + \frac{2\ell_m \sin\theta}{\lambda} \right) \right\} \tag{2}$$

where $s_{if}(t, m)$ is the received raw intermediate frequency signal by the radar at m^{th} step on the GBSAR's along-track, and similar to MIMO radar, ℓ_m is the virtual antenna location on the azimuth or along-track axis, which is acquired during sensor's movement on its trajectory.

2.2. Problem statement and signal model

In the preceding sections, the raw signal that was received did not yet reveal the locations and characteristics of the scatterers. Additionally, the raw signal has a low signal-to-noise ratio (SNR). Consequently, in order to identify scatterers along the parameters of interest, it becomes necessary to focus the raw signal towards that specific direction. This task can be accomplished through signal processing techniques, particularly using matched filtering approaches. In radar imaging, the relative location of scatterers from the radar is determined by their range (r) and cross-range angle (θ). Moreover, our intention is to detect displacement characteristics of the targets alongside their location parameters. Thus, we are confronted with a multi-dimensional imaging problem that entails determining the location and displacement characteristics of the scattering targets.

The signal focusing in range direction is achieved by performing matched filtering partially within the radar sensor. This involves convolving the received signal with a time-reversed replica of the transmitted chirp using a mixer. After applying band-pass filtering, the resulting dechirped intermediate frequency signal s_{if} (shown in (1) and (2)) is obtained. Subsequently, by performing a Fourier transform, we obtain the range-focused (or range-compressed) data. Therefore, the range-compressed data of N_r recorded range samples at the q^{th} acquisition of m^{th} virtual receiver can be derived from the Fourier transform of the received signal as follows: $s_{rc} = \mathscr{F}_r\{s_{if}\}$. Consequently, each bin on the acquired range profile directly corresponds to a specific pixel's range. More details regarding radar's range compression can be found in [38]. Hence, we can modify the raw signal model, as shown in equations (1) and (2), to a general frequency domain signal model that represents the distribution of received signals from different cross-range points. This is applicable to the r^{th} range bin of the range-compressed signal in MIMO or SAR imaging mode as follows

$$s_{rc} = \int_{\theta} \gamma(\theta) \cdot e^{-j\frac{\alpha 2\pi}{\lambda}(\ell_m \sin\theta)} d\theta \tag{3}$$

where γ is the function modelling the scattering distribution, and $\alpha = 1$ and 2 for multi-static MIMO and mono-static SAR signals, respectively [36,37,39].

The signal model presented in (3) serves as the initial framework for multi-dimensional imaging. It represents the simplest scenario where the scattering targets are assumed to remain stationary during data acquisition. Fig. 2 shows the proposed processing chain for

multi-dimensional detection of scatterers from radar signals using SE techniques. The processing chain begins with range compression, followed by the application of the algorithm to each range bin of the data. For every range bin, the estimated covariance matrix is convolved with the determined system matrix to estimate the power spectrum in the domain of parameters, such as azimuth AoA, linear velocity, vibrational amplitude, and frequency. Next, the power spectrum obtained through the SE method is inputted into the CLEAN algorithm. The CLEAN algorithm iteratively suppresses sidelobes and background noises, enhancing the accuracy of the estimated power spectrum. By repeating the entire process for all range bins and stacking the estimated power spectra, a multi-dimensional cube is generated. This cube resembles a focused image in the parameter domain.

Assuming that the scattering target is undergoing linear motion during the data acquisition, an additional displacement term must be included in the model described by equation (3) in order to account for the contributions of the scatterers' LOS linear displacement velocity (v) and azimuth AoA (θ). Thus, at data acquisition time of $T_q = qt_p$, additional phase term $2\pi T_q v/\lambda$ is added to the collected signals, where t_p is the data acquisition interval (or periodicity). Thus, the modified model is as follows

$$s_{rc} = \iint_{\chi} \gamma(\boldsymbol{\chi}) \cdot e^{-j\frac{q2\pi}{\lambda}(\ell_m \sin\theta)} \cdot e^{-j\frac{2\pi}{\lambda}T_q v} d\theta dv \tag{4}$$

The above equation can also be named as Azimuth-Velocity differential signal model, where $\gamma(\boldsymbol{\chi})$ is the function modelling the scattering distribution along the space of unknown $\boldsymbol{\chi} = [\theta, v]$.

The vibrational displacement can be modeled with sinusoidal function. Hence, the vibration signal can be represented by $\xi\sin(2\pi\eta T_q + \varphi)$, where ξ is the amplitude of the target's vibration, η denotes vibration frequency, and φ is the vibration signal's initial phase. Thus, in case of having vibrational displacement behavior, the multi-dimensional signal model can be reformulated as an Azimuth-Vibration differential signal model:

$$s_{rc} = \int\int\int\int_{\chi} \gamma(\boldsymbol{\chi}) \cdot e^{-j\frac{q2\pi}{\lambda}(\ell_m \sin\theta)} \cdot e^{-j\frac{2\pi}{\lambda}\xi\sin\left(2\pi\eta T_q+\varphi\right)} d\theta d\xi d\eta d\varphi \tag{5}$$

In this case, three parameters are added to model the target's sinusoidal vibration in the radar's LOS direction. Thus, for multi-dimensional modelling of Azimuth AoA and vibrational displacement, the unknown variables' vector is defined as $\boldsymbol{\chi} = [\theta, \xi, \eta, \varphi]$ [40].

Thus, as it is also shown in Fig. 3, the generalized multi-dimensional SAR modelling of azimuth AoA, and linear and non-linear displacements can be defined as follows

$$s_{rc} = \int\int\int\int\int_{\chi} \gamma(\boldsymbol{\chi}) \cdot \underbrace{e^{-j\frac{q2\pi}{\lambda}(\ell_m \sin\theta)}}_{\text{AOA term}} \cdot \underbrace{e^{-j\frac{2\pi}{\lambda}T_q v}}_{\text{Linear velocity term}} \cdot \underbrace{e^{-j\frac{2\pi}{\lambda}\xi\sin\left(2\pi\eta T_q+\varphi\right)}}_{\text{Nonlinear vibration term}} d\theta dv d\xi d\eta d\varphi \tag{6}$$

where the unknown parameters are represented in a five-dimensional vector $\boldsymbol{\chi} = [\theta, v, \xi, \eta, \varphi]$.

2.3. Spectral estimation and inversion model

During data acquisitions, the radar samples can be distributed along the azimuth axis either regularly or irregularly. This distri-

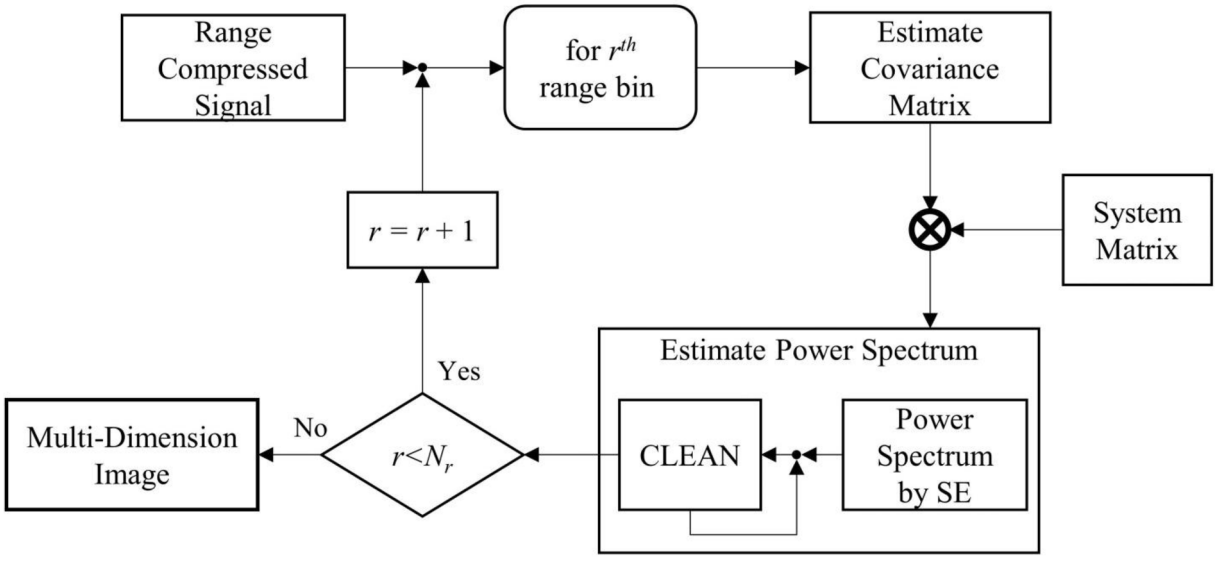

Fig. 2. Flowchart of the processing chain for multi-dimensional imaging using the proposed imaging modes.

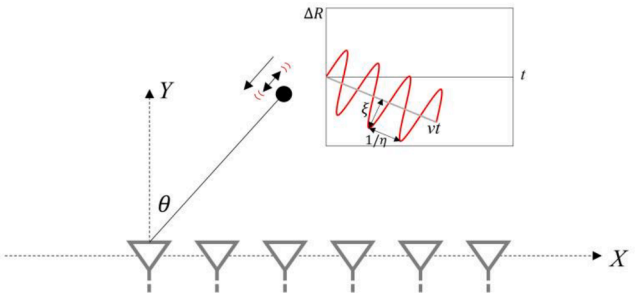

Fig. 3. Azimuth angle of arrival and displacement model of a point scatterer in radar's imaging geometry.

bution depends on the virtual antenna geometry in MIMO imaging mode or the sensor trajectory in GBSAR imaging mode. To address this, we discretize the signal models defined in equations (4–6) at K points. These points correspond to the discrete samples within the domain of interest in the parameter vector's $\boldsymbol{\chi}$ hyperplane. As a result, the problem transforms into a matrix problem [29]:

$$\mathbf{x} = \mathbf{A}\boldsymbol{\gamma} + \mathbf{n} \tag{7}$$

where,

- $\mathbf{x} \in \mathbb{C}^{N\times 1}$ is a vector obtained from all the pixels in the r^{th} range bin of the bins of the measured range-focused signal (s_{rc}), where in the case of MIMO radar data acquisition mode (8a), $N = N_a \times N_q$, and in the case of SAR data acquisition mode (8b), $N = N_a$, and the operator vec() stacks the matrix columns one after the other.

$$\mathbf{x} = vec\{s_{rc}(r)\} \quad \text{(MIMO)} \tag{8a}$$

$$\mathbf{x} = s_{rc}(r) \quad \text{(SAR)} \tag{8b}$$

- $\mathbf{n} \in \mathbb{C}^{N\times 1}$, $\mathbf{n} \sim N\ (0,\ \sigma)$ is the complex additive white noise that follows a Gaussian distribution with zero mean and standard deviation of σ.
- $\boldsymbol{\gamma} = [\gamma_0, \ldots, \gamma_{K\text{-}1}]^T \in \mathbb{C}^{K\times 1}$ is collected from the values of the backscattered signals at K discrete bins.
- $\mathbf{A} = \sqrt{N}[\mathbf{a}_0, \cdots, \mathbf{a}_{K-1}] \in \mathbb{C}^{N\times K}$ is sensing (system) matrix, collected from the $\mathbf{a}_k$ $N \times 1$ steering vectors

The steering vector in the case of azimuth AoA and linear displacement velocity estimation for (θ_i, v_j) discrete bins is defined as follows:

$$\mathbf{a}_k = \mathbf{a}_k(\theta_i, \nu_j) = \frac{\exp\left\{ -j\frac{2\pi}{\lambda}\left(\alpha \boldsymbol{L}\sin\theta_i \oplus \boldsymbol{T}\nu_j\right)\right\}}{\sqrt{N}} \tag{9}$$

where,

- $\mathbf{L} = [\ell_0, \ell_1, \ldots, \ell_{Na\text{-}1}]$ is the vector containing radar's azimuth locations
- $\mathbf{T} = [T_0, T_1, \ldots, T_{Nq\text{-}1}]$ is the vector containing signal acquisition times, where in our suggested data acquisition modes, $T_q = qt_p$, $q = 0, 1, \ldots, N_q - 1$, and t_p denotes 2D range-azimuth data acquisition interval in MIMO mode and 1D range profile acquisition interval in SAR mode.

Similarly, the steering vector in the case of azimuth AoA and vibrational displacement estimation for (θ_i, ξ_j, η_k, φ_l) discrete bins can be defined as follows:

$$\mathbf{a}_k = \mathbf{a}_k(\theta_i, \xi_j, \eta_k, \varphi_l) = \frac{\exp\left\{ -j\frac{2\pi}{\lambda}\left(\alpha \mathbf{L}\sin\theta_i \oplus \xi_j \sin(2\pi\eta_k \mathbf{T} + \varphi_l)\right)\right\}}{\sqrt{N}} \tag{10}$$

In our presented SAR data acquisition mode, it is worth noting that **L** and **T** are obtained in the same dimensional space, resulting in them having the same dimensions. However, in the MIMO data acquisition mode, during each epoch of data acquisition, we have full azimuth samples. As a result, the **L** and **T** vectors have different dimensions, and they are orthogonal to each other. To address this, we define a general form for the vector summation operator $\oplus$ in equations (9) and (10), as shown in equation (11).

$$\begin{aligned} &[x_1, \cdots, x_m]^T \oplus [y_1, \cdots, y_m]^T = [x_1 + y_1, x_2 + y_2, \cdots, x_m + y_m]^T_{1\times m} \\ &[x_1, \cdots, x_m]^T \oplus [y_1, \cdots, y_n]^T = [x_1 + y_1, x_1 + y_2, \cdots, x_2 + y_1, \cdots, x_m + y_n]^T_{1\times(m\times n)} \end{aligned} \tag{11}$$

To solve $\boldsymbol{\gamma}$ or $\mathbf{P}$ by inversing the linear model in (7), first we need to estimate the covariance matrix of observations. The covariance matrix of the observed signal is

$$\begin{aligned}\mathbf{R} = E\{\mathbf{x}\mathbf{x}^H\} &= E\{(\mathbf{A}\boldsymbol{\gamma}+\mathbf{n})(\mathbf{A}\boldsymbol{\gamma}+\mathbf{n})^H\} \\ &= E\{(\mathbf{A}\boldsymbol{\gamma}+\mathbf{n})(\boldsymbol{A}\boldsymbol{\gamma}+\mathbf{n})^H\} \\ &= \mathbf{A}E\{\boldsymbol{\gamma}\boldsymbol{\gamma}^H\}\mathbf{A}^H + E\{\mathbf{n}\mathbf{n}^H\} \\ &= \mathbf{A}diag\underbrace{\{\boldsymbol{\gamma}^2\}}_{\mathbf{P}}\mathbf{A}^H + \sigma^2\mathrm{I}_N\end{aligned} \tag{12}$$

where the superscript $(.)^H$ denotes Hermitian transpose, $E\{.\}$ and $diag\{.\}$ are the expectation and diagonal operators, respectively, $\mathbf{I}_N$ is $N \times N$ identity matrix, and $\mathbf{P}$ is the reflectivity power spectrum [26,41]. Notably, assuming that reflectivity values are uncorrelated, the off-diagonal values of $\boldsymbol{\gamma}\boldsymbol{\gamma}^H$ will be zero and only the diagonal elements will be non-zero.

The estimation of sample covariance matrix ($\mathbf{R}\hat{}$) can be attained by local spatial averaging of the observed signals in the range compressed signal s_{rc}, in a range window around the range bin under analysis:

$$\widehat{\boldsymbol{R}} = n_r^{-1}\sum_{r=1}^{n_r}\mathbf{x}(r)\mathbf{x}(r)^H \tag{13}$$

where n_r is the size of the range window.

Spectral estimation technique concerns estimating power spectrum from inverting the (10). The classic approach for this purpose is Beamforming (BF) algorithm, which is a nonparametric approach that estimates scatterer reflectivity power by increasing the signal's SNR based on matched filtering [21,29,30]. BF estimates the power spectrum by inversing (12) as follows:

$$\widehat{P}(\boldsymbol{\chi}) = \mathrm{diag}\{\mathbf{A}^H\widehat{\mathbf{R}}\mathbf{A}\} \tag{14}$$

Although the obtained power spectrum through BF is more robust to noise than Fourier analysis [21], it is possible to attain poor performance in terms of sidelobes and leaked point spread function due to sparse and non-uniform data acquisitions [19]. Hence, alternative spectral estimation methods such as nonparametric data adaptive Capon filter and parametric multiple signal classification (MUSIC) are more recommended in the literature [21].

Capon beamformer has practically shown better performance than conventional BF in high resolution scatterer spectral unmixing and sidelobe suppression [21,42]. The Capon power estimation is as follows:

$$\widehat{P}(\boldsymbol{\chi}) = \left(\mathbf{a}_k^H(\boldsymbol{\chi})\mathbf{R}^{-1}\mathbf{a}_k(\boldsymbol{\chi})\right)^{-1} \tag{15}$$

MUSIC aims to retrieve a finite source of signals (scatterers) D from a relatively large number of observations ($D \ll N$) by computing the noise subspace $\mathbf{E}_n$ obtained from the subspace decomposition of the sample covariance matrix (13). The subspace $\mathbf{E}_n$ is associated with the $N - D$ smallest eigenvalues of the covariance matrix, which are known as noise Eigenvectors and are basically orthogonal to the signal Eigenvectors. Thus, the number of scatterers (D) needs to be set in the MUSIC algorithm [21]. According to the literature, the MUSIC estimator has provided improvements in detecting point-like scatters especially in urban areas [19,43]. The power spectrum of MUSIC is obtained as follows:

$$\widehat{P}(\boldsymbol{\chi}) = \left(\mathbf{a}_k^H(\boldsymbol{\chi})\mathbf{E}_n\mathbf{E}_n^H\mathbf{a}_k(\boldsymbol{\chi})\right)^{-1} \tag{16}$$

Therefore, the scatterers position vector $\overline{\chi}_i$ in the multi-dimensional search space of parameters can be identified by finding the peak power in the estimated power spectrum [19]:

$$\widehat{\boldsymbol{\chi}}_i = \underset{\boldsymbol{\chi}}{\mathrm{argmax}}\{\widehat{P}(\boldsymbol{\chi})\} \tag{17}$$

The process of estimating the reflectivity values by a spectral estimator is performed for each range bin of the range compressed signal, in which the present scatterers are detected. Subsequently, the stack of scatterers in all the range bins results in a multi-dimension image realizing the range and AoA of scatterers, as well as their displacement characteristics, which are linear velocity, and vibration frequency and amplitude. The presented steps are summarized in Algorithm 1.

Algorithm 1. Multi-dimensional imaging based on SE

Input: Range-compressed SAR or time-series MIMO signal
Output: Multi-dimensional image of unknown parameters
1- Compute system matrix **A** from the stack of steering vectors as shown in (9) for linear velocity and (10) vibration
2- for each $r^{\mathrm{th}} \in \mathbb{N}$, $r \leq N_r$ range bin ($\mathbf{x}$) as shown in (7):
a) Estimate covariance matrix as shown in (13)
b) Estimate the power spectrum based on one of the SE methods shown in (14)-(16)
c) Identify the parameter values of dominant scatterers by finding the location of maximum values as shown in (17).
3- Stack estimated power spectrums in range direction to form a multi-dimensional image, where each axis refers to an unknown parameter.

2.3.1. Background and noise suppression with CLEAN algorithm

The CLEAN algorithm [44,45] is utilized as a post-processing technique to diminish the impact of background, signal interferences, and sidelobes on the initially estimated power spectrums. The main concept involves identifying the position and intensity of point sources and progressively removing their contribution from the estimated power spectrum. This iterative approach effectively reduces the influence of the background and undesired signals, referred to as the 'dirty' image. On the other hand, due to the known position and strength of the deconvolved source, point sources with the appropriate strength are placed into the 'clean' image. Upon completing the iterations, the final power spectrum is formed by convolving the clean components with an ideal beam and adding the residual image. Previous studies have demonstrated the effectiveness of this algorithm in various waveforms such as acoustic [46], infrasound [47], and seismic [48] even when the number of receiver arrays is limited.

In each iteration, the CLEAN algorithm selects the main contribution in the initially estimated spectrum by one of the SE methods brought in (14–16) and removes a percentage of the corresponding signal from the sample covariance matrix ($\mathbf{R}\hat{}$):

$$\mathbf{R}_i = \mathbf{R}_{i-1} - \omega D^{-1} \sum_{j=1}^{D} \widehat{P}(\boldsymbol{\chi}_j)\mathbf{a}(\boldsymbol{\chi}_j)\mathbf{a}(\boldsymbol{\chi}_j)^H \tag{18}$$

where $\mathbf{R}_i$ is the updated covariance matrix at i^{th} iteration of the algorithm, D is the number of targets, χ_j is the location of the j^{th} target obtained by finding the first D strongest peak points from the initial power spectrum, and $0 < \omega < 1$ is the control parameter that determines the fraction of removed power. In this procedure, the array response is deconvolved from the resolved power spectral density function. The spectral peaks are retained in a 'clean' spectrum:

$$P_{CLEAN}(\boldsymbol{\chi}) = \omega D^{-1} \sum_{i=1}^{Q} \sum_{j=1}^{D} \widehat{P}(\boldsymbol{\chi}_j)_i \tag{19}$$

After finishing the iterations, the final improved power spectrum is obtained by adding the residual power spectrum at final iteration (P_Q), which is estimated based on the updated covariance matrix in (18) and the clean power spectrum obtained in (19):

$$\widehat{P}(\boldsymbol{\chi}) = \widehat{P}_Q(\boldsymbol{\chi}) + P_{CLEAN}(\boldsymbol{\chi}) \tag{20}$$

The stopping criteria for the iterations can be user defined, or stop if the degraded covariance contains more information than in the previous iteration [45] or when the peak in the residual image reaches a level comparable with the theoretical noise [48].

3. Experiments and results

In this section, various numerical simulations and experimental studies have been conducted to evaluate the effectiveness of the proposed monitoring systems. Both MIMO radar and GBSAR imaging modes have been investigated in terms of their capability to detect multiple scatterers with high resolution in multiple dimensions. The results have been evaluated using two popular metrics: signal-to-noise ratio (SNR), which indicates the noise level of the obtained power spectrum, and peak-to-sidelobe ratio (PSLR), which represents the ratio between the peak power of targets and the undesired sidelobes or grating lobes in the vicinity of the target in the power spectrum. These metrics have been calculated using the following formulas:

$$SNR = 10\log_{10}\left(\frac{\sum_{i=1}^{D} P_i}{D\sigma_P}\right) \tag{21}$$

$$PSLR = 10\log_{10}\left(\frac{P_i}{Q_i}\right) \tag{22}$$

where P_i and Q_i are the estimated power of the i^{th} scatterer and its closest sidelobe, and σ_P is the standard deviation of the estimated power spectral density (PSD).

3.1. Experiments and analysis on simulated data

The numerical simulations were carried out by simulating the signal and parameters of Texas Instrument's TI-AWR1642 radar sensor [49]. This sensor operates at W-band (76 – 81 GHz) with millimeter scale wavelength. It consists of two transmitter antennas with 2λ spacing and four receiver antennas with $\lambda/2$ in MIMO geometry, which results in eight virtual arrays with $\lambda/2$ spacing. For GBSAR imaging scenario, a monostatic radar sensor with the same signal parameters as the MIMO radar but moving on a linear aperture with 2.5 cm/s speed was considered. Table 1 shows the full list of parameters used for simulating MIMO radar and GBSAR imaging mode.

Table 2 shows the simulated scenarios for multi-dimensional scatterer separation from MIMO radar or GBSAR imaging modes. Three scattering targets located at the same slant range (20 m) but with different cross-range locations and displacement characteristics were simulated in each scenario. According to the parameters shown in Table 1, the length of the obtained virtual aperture from

MIMO radar processing is $L=(N_{Tx} \times N_{Rx}) \times \lambda/2 = 1.52$ cm, providing cross-range resolution of $\delta_\theta = \lambda/L = 0.0038/0.015 \approx 0.25$ rad. In contrast, in the case of GBSAR imaging, it is feasible to deploy a mechanical rail up to few meters long in most of the currently available systems [50]. However, as mentioned, this feature provides a better cross-range resolution at a cost of several minutes of the data acquisition time. In this study, we simulated a GBSAR system with 15 cm virtual aperture length, leading to the cross-range resolution of $\delta_\theta = \lambda/L = 0.0038/0.15 \approx 0.025$ rad. MIMO radar provides a fixed number of virtual antennas. In this case, Time-division multiplexing (TDM) processing of MIMO signals with 60 μs chirp duration (see Table 1) can provide a millisecond scale data acquisition interval from all the antennas [51]. Thus, in the simulated scenarios, the data acquisition interval was set to be 0.02 s, which indicates the repetition time for each range-azimuth data acquisition. In the case of GBSAR imaging, the acquisition interval for each range profile during the radar's movement on its trajectory was set to 0.02 s.

The evaluation results of the simulations are presented in Table 3. The Fourier Transform (FT), which serves as the base and conventional method, exhibits the lowest performance (SNR = 11.46 dB) compared to the other estimators. Furthermore, it is only applicable for linear velocity estimation from MIMO measurements and cannot be applied to SAR measurements. On the other hand, the other implemented spectral estimation (SE) methods, based on the proposed signal models, demonstrate improved results with higher SNR. Regarding the CLEAN algorithm, to minimize processing time, we set ω to 0.9 and utilized 5 iterations. The effectiveness of the CLEAN algorithm is evident in effectively suppressing background power and significantly increasing the SNR of the estimated PSDs. For example, the SNR level of the results obtained by MUSIC increases from 17 to 19 dB to 31–32 dB in all cases. It is worth noting that the CLEAN algorithm exhibits better improvement when used with advanced estimators such as Capon or MUSIC, rather than BF. This could be attributed to the capability of these methods to generate higher resolution initial PSD images, as well as their higher sensitivity to a clean covariance matrix compared to BF.

Fig. 4 shows the estimated PSDs by Capon method for the velocity monitoring scenario. In this scenario, range profiles were acquired in a linearly back-and-forth repeat-pass (zigzag) manner with maximum aperture length of 3 cm in the GBSAR's along-track direction for SAR imaging mode. This non-linear trajectory approach enables the proposed algorithm to separate the linear displacement characteristics of scatterers, as well as their high-resolution cross-range angle of arrival (more analysis on the effect SAR trajectory is discussed in the next section). The improvement by the CLEAN algorithm is also evident from the presented PSDs, where the signal power of the background is much lower and more homogeneous after its application. Specifically, the obtained PSD from the MIMO radar signal after performing the CLEAN algorithm provides sharper and narrower peak signals from the targets' location. On the other hand, the sidelobes obtained due to the back-and-forth trajectory of the SAR appear on the PSD by Capon, significantly reducing the SNR and target discriminability of the image. However, it can be observed that after performing the CLEAN algorithm, the effect of the SAR trajectory has been considerably reduced.

Fig. 5 shows the obtained simulation results of estimating vibrational displacement parameters based on the proposed approach by Capon estimator. As brought in the Methodology section, the AoA-vibration estimation problem involves four variables, including azimuth AoA θ, vibration amplitude ξ, vibration frequency η, and vibration phase shift φ. With the exception of the phase shift parameter, which is a number in $[0, \pi]$, the three estimated main parameters can be shown in three images, including the surfaces of θ-η, θ-ξ, and ξ-η. The results exhibit strong and distinctive reflectivity in the locations of the simulated targets. Thanks to the longer aperture length in SAR imaging mode, we can observe sharper impulse responses in AoA axis (θ), which demonstrates better cross-range resolution and more accurate localization of scatterers. However, similar to the velocity estimation scenario, the CLEAN algorithm significantly suppresses the background and reduces the sidelobes, particularly in the case of MIMO radar imaging, where the obtained peak signals appear to be narrower and closer to the results obtained by SAR signals.

Regarding the performance comparison of MIMO and SAR imaging modes, it can be noticed that both cases provided similar results in terms of SNR of the estimated PSDs in both scenarios of estimating linear velocities and vibration parameters. However, as mentioned earlier, SAR enables higher cross-range resolution by possessing a longer aperture length rather than MIMO radar. In fact, Despite the strong capabilities of the utilized estimators in suppressing background signals, long aperture is still required to distinguish closely located scatterers. As can also be observed from Fig. 4 and Fig. 5, peak signals appear narrower along the AoA axis (θ) for SAR results. Therefore, the simulated experiments validate the applicability of the proposed approach for high-resolution detection of sub-second scale displacements using SAR signals, and improving the target detection capability of low-resolution MIMO radars by reducing the effects of sidelobes and suppressing the background signal.

In order to further analyze the robustness and applicability of the proposed methodology, the performance of each imaging modes

Table 1
System specifications for simulated experiments.

Parameter	Value
Starting frequency (f_0)	77 GHz
Signal wavelength (λ)	0.0038 m
Signal bandwidth (b_w)	1 GHz
Signal SNR	5 dB
Chirp duration (τ)	60 μs
Radar's range resolution	0.15 m
MIMO radar transmitters (N_{Tx})	2
MIMO radar receivers (N_{Rx})	4
MIMO radar Virtual antennas	8
Sensor's along-track speed on rail	2.5 cm/s

Table 2
Data acquisition characteristics of the simulated experiments.

Monitoring Scenario	Imaging mode	Aperture length (mm)	Signal acquisition interval (s)*	Total time of Acquisition (s)	Targets' characteristics**
Linear velocity	MIMO	15.2	0.02	2	r = [20, 20, 20] θ = [-20, 0, 10]
	SAR	30	0.02	6	v = [-15, 0, 5]
Vibration	MIMO	15.2	0.02	2	r = [20, 20, 20] θ = [-10, 0, 20]
	SAR	150	0.02	6	ξ = [5, 1, 2] η = [7, 2,0.4]

* Here, the definition of "signal acquisition interval" for MIMO radar imaging is the repetition time for acquiring full range-azimuth data, and for the GBSAR imaging is the repetition time for the acquisition of each range signal.

** r denotes simulated targets' range in m, θ denotes targets' azimuth angle in deg, v is the targets' linear velocity in mm/s, ξ denotes vibration amplitude of targets in mm, and η denotes vibration frequency of targets in Hz.

Table 3
Evaluation results of simulated experiments (Numbers are in dB).

Monitoring scenario	Imaging mode	BF		Capon		MUSIC		FT
			CLEAN		CLEAN		CLEAN	
Linear velocity	MIMO	15.49	15.91	16.74	26.92	17.35	31.03	11.46
	SAR	16.38	17.21	18.27	31.48	19.48	33.24	–
Vibration	MIMO	17.73	18.03	17.91	32.8	18.39	32.51	–
	SAR	17.32	17.87	17.39	30.33	18.45	31.37	–

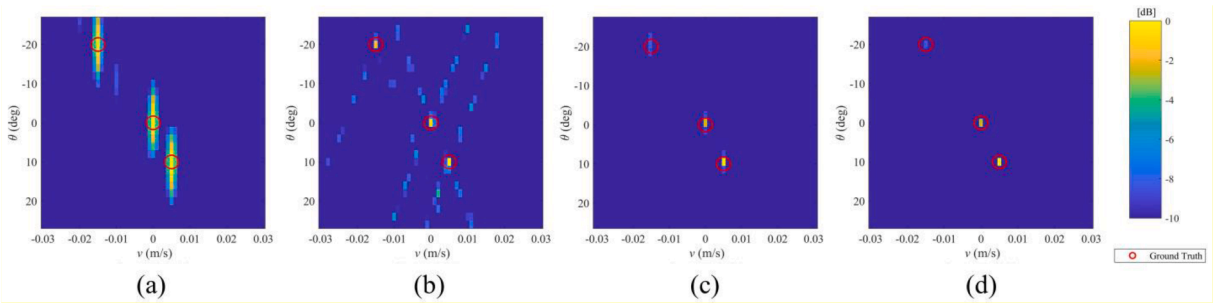

Fig. 4. Comparison of imaging modes' azimuth and velocity retrieval from simulated experiments by Capon estimator: a) MIMO, b) SAR, c) MIMO after CLEAN algorithm, d) SAR after CLEAN algorithm.

was assessed under various conditions, including the different noise levels in the received signal (power of received signal to the power of noise), different number of scattering targets in one range bin, and different length of synthetic aperture for SAR imaging scenario. Fig. 6 shows the SNR of the estimated multi-dimensional PSD by Capon estimator, based on MIMO radar measurements for the vibration monitoring scenario, with different noise levels on the received signal, ranging from −50 to 0 dB, and for the presence of 1 to 5 scatterers in a range bin. As can be observed, reducing the noise level improves the SNR of the obtained PSD. On the other hand, increasing the number of scatterers in one cell yields to lower SNR of the estimated PSD. This can be due to the increasing the effect of interference of backscattered powers from the multiple scatterers. However, as depicted in Fig. 6 (b), applying the CLEAN algorithm caused a significant increase in the SNR of the estimated PSDs, even with a noise level of −30 dB and in the presence of 5 scatterers in one range bin. Hence, based on this analysis, one can infer that although the effectiveness of the proposed method on MIMO radar is affected by the quality of the received signals and the number of scatterers, combining it with CLEAN algorithm and leveraging its background suppression capability can considerably improve the method's robustness and applicability on MIMO radar measurements.

In case of SAR imaging mode, Fig. 7 illustrates the effects of aperture length, noise level, and number of scatterers in a range bin on the PSD estimation of vibration parameters by the proposed method and Capon estimator. According to the results, a high level of signal noise (e.g., −50 dB) in all cases of aperture length and number of scatterers results in a PSD with weak SNR close to 0 dB, where the targets' peak point cannot be discriminated from the background. On the other hand, increasing the aperture length could slightly improve the SNR, mainly due to the increase in cross-range resolution. Similar to the results obtained by MIMO radar measurements, increasing the number of scatterers reduces the SNR, mainly due to the interference of scatterers in one range signal bin. However, comparing the MIMO and SAR results shows a higher SNR of SAR imaging mode under the same conditions, which can be attributed to the better angular discriminability caused by the better resolution of SAR. Additionally, the positive effect of the CLEAN algorithm is

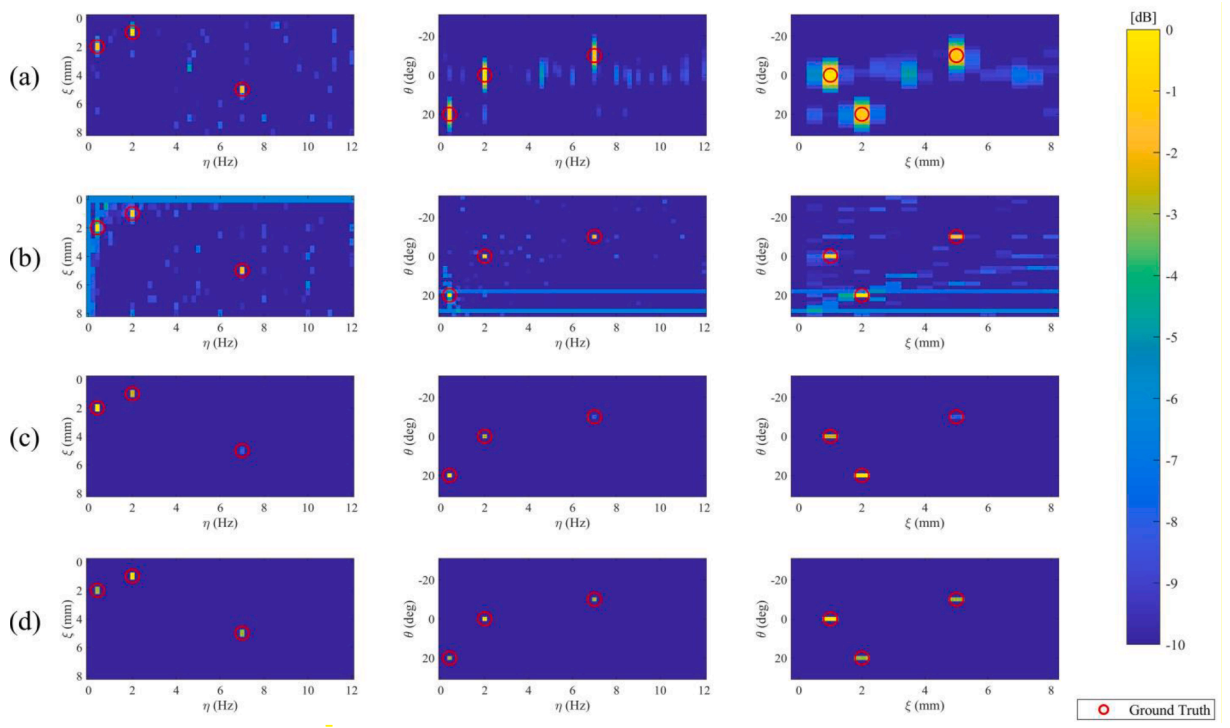

Fig. 5. Comparison of imaging modes' azimuth and vibration retrieval from simulated experiments by Capon estimator: a) MIMO, b) SAR, c) MIMO after CLEAN algorithm, d) SAR after CLEAN algorithm.

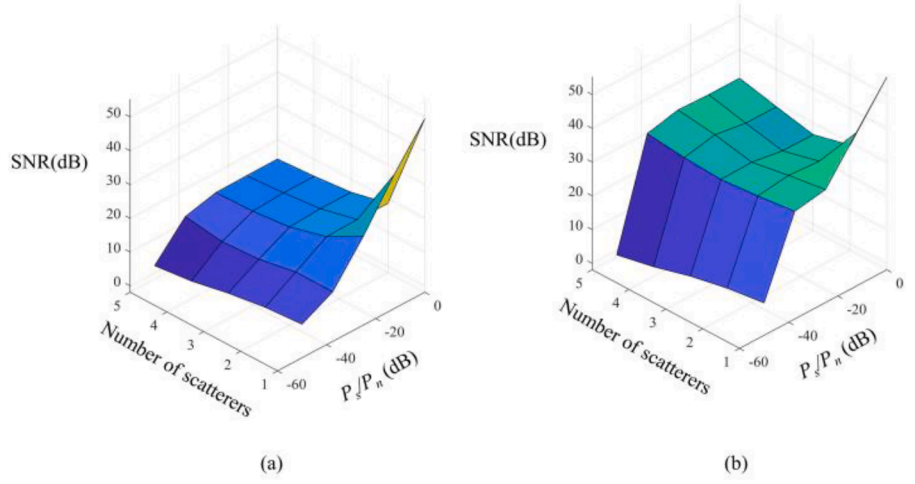

Fig. 6. Analysis on the effect of noise level, and number of targets in a range bin on velocity estimation from MIMO radar signals based on a) Capon, b) Capon + CLEAN.

demonstrated, where it can reduce the effects of background and target interferences and improve the SNR even when the number of scatterers and noise level is high. However, it should be noted that from both experiments on MIMO and SAR imaging modes, CLEAN cannot be effective when the resulting SNR of PSD is very low and close to zero. This is due to the fact that the CLEAN algorithm requires accurate localization of scatterers in the PSD during its iterative process, and thus, a higher initial estimated SNR of scatterers leads to a better localization and better improvement by CLEAN.

In another experiment, we analyzed the effect of the SAR trajectory on estimating the displacement parameters. The main motivation for this experiment comes from the fact that in spaceborne SAR processing, it is a common approach to use repeat-pass observations with irregularly distributed baselines to resolve scatterers' height or displacement [25,29]. However, in our demonstrated problem, it is not feasible to achieve irregular baselines in the azimuth direction because the data acquisition interval between each

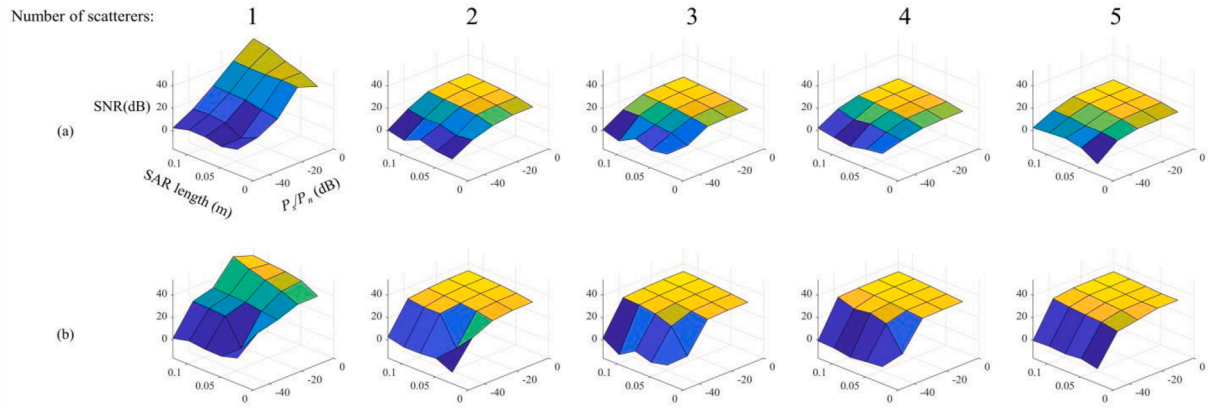

Fig. 7. Analysis on the effect of noise level, SAR length, and number of targets in a range bin on vibration estimation from SAR signals based on a) Capon, b) Capon + CLEAN.

range signal needs to be very short to estimate sub-second displacements accurately. Thus, it is essential to find out how to define the SAR trajectory to obtain results as close as possible to the ideal but physically impossible irregular baseline. To this end, we analyzed two SAR trajectories, including a linear and back-and-forth repeat-pass trajectory in the form of a zigzag, as well as the randomly distributed (irregular) trajectory as the base approach.

Table 4 shows the performance evaluation of the implemented scenarios for each trajectory. According to the results, the irregular trajectory obtained the highest SNRs in all cases, as we expected. However, in the case of the linear trajectory, it is noticeable that it obtained poor results for linear velocity estimation. It can also be inferred from the poor results of the CLEAN algorithm for this scenario, which means that the linear trajectory could not correctly separate and focus scatterers in the resulting PSDs. The main reason could be due to the interference of the linear phase shift caused by both the SAR linear trajectory and scatterers' linear movement. This results in a coherent uniform summation during the data acquisition, which reduces the possibility of decomposing the effect of the SAR trajectory from the scatterers' linear displacement. On the other hand, for vibration monitoring, both linear and zigzag trajectories obtained results close to the base irregular trajectory. The main reason for these results could be the nonlinear displacement nature of vibrations, which makes it possible to utilize linear SAR.

The visual comparison of AoA-velocity PSDs estimated by Capon for each type of investigated trajectory is shown in Fig. 8. It can be observed that the random (irregular) trajectory obtained the most appealing results with a dark background. However, in the case of the linear trajectory, the SAR movement put linear traces with strong power on the PSD, making it difficult to obtain the targets' accurate location. This issue is considerably solved by utilizing the zigzag trajectory. In this case, the effect of the SAR trajectory is dampened on the PSD, while the targets appear with strong and distinctive power. Furthermore, due to the reduction of the power of SAR trajectory's traces on the PSD, adding the CLEAN algorithm resulted in a strong suppression of the background and effects of SAR trajectory. Similarly, Fig. 9 shows the estimated PSDs for vibration monitoring with different SAR trajectories. As is observable, both linear and zigzag trajectories presented PSDs close to the irregular trajectory scenario, where the targets' locations are correctly estimated with strong powers with respect to their surrounding background. However, due to the shorter aperture length in the zigzag trajectory, the azimuth resolution is lower than the linear trajectory, and thus the estimated targets appear wider in the AoA axis.

The summary of applicability of different investigated trajectories is provided in Table 5. Although the linear trajectory is the most common approach for SAR imaging, it is not applicable for linear velocity estimation purposes. The zigzag trajectory has been shown to be applicable for both vibration and velocity estimation applications. However, it is worth noting that the main drawback of the zigzag trajectory is its shorter aperture length for the same data acquisition duration compared to the linear SAR, which is inevitable in the case of velocity monitoring.

3.2 Real experiments

Table 4
Evaluation results of the experiments on the effect of SAR trajectory on the estimated power spectrum densities (Numbers are in dB).

Monitoring scenario	Estimator	Irregular (physically not possible)		Linear		Zigzag (continuous repeat-pass)	
			CLEAN		CLEAN		CLEAN
Linear velocity	BF	18.51	21.54	14.51	15.04	14.98	15.35
	Capon	18.78	36.06	16.78	17.27	16.46	31.14
	MUSIC	19.92	34.37	17.32	22.15	17.39	31.96
Vibration	BF	18.34	21.02	17.60	18.82	17.26	18.45
	Capon	18.46	31.97	18.10	31.38	17.60	30.61
	MUSIC	19.64	33.18	19.18	32.57	18.55	32.03

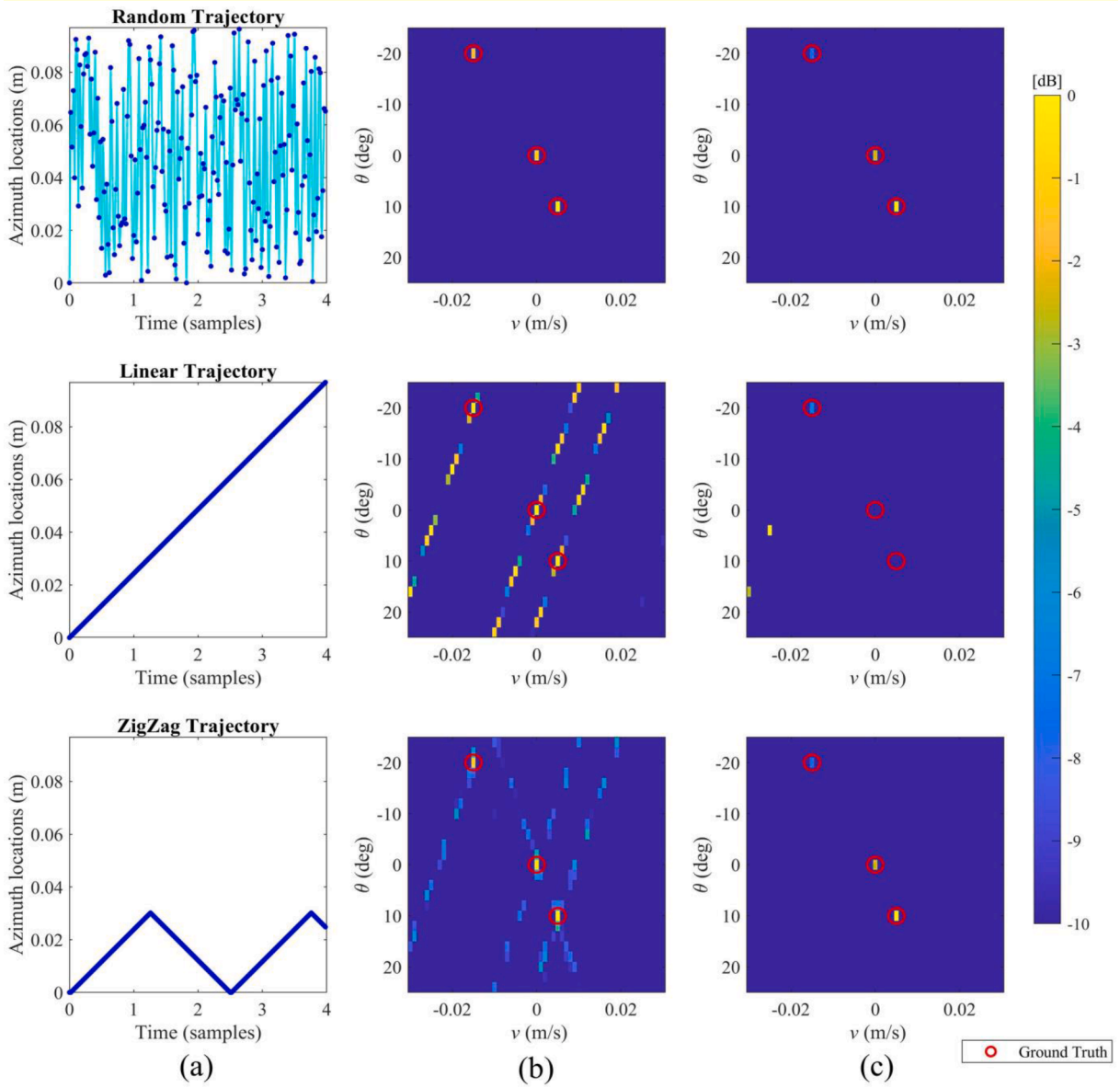

Fig. 8. Power spectrum densities for linear displacement monitoring for different SAR trajectories by estimator: a) SAR trajectory, b) Capon, c) Capon + CLEAN.

In this section, experiments from real data are reported to verify the efficiency of the proposed method. To this aim, we employ our developed GBSAR system, consisting of a radar sensor mounted on a two-dimensional mechanical rail. The radar sensor continuously moves on the horizontal axis with a controllable velocity of up to 4 cm/s. Also, step-wise movement with a fixed offset on the vertical axis can be attained after each radar's horizontal scan to provide a two-dimensional synthetic aperture. However, only the signals obtained from one horizontal scan are required in this study. The full description and details of our developed GBSAR system are available in [33]. The radar sensor used on this system is Texas Instrument's AWR1642. This sensor has also MIMO imaging capability with eight virtual arrays (see Table 1).

Fig. 10-a shows the experimental setup for the performance evaluation of the proposed methods. The radar sensor is pointed at a scene, including four corner reflectors (CR). One CR is mounted on a linear stage with micro-meter accuracy and is programmed to move during the data acquisition time, while the other CRs remain fixed. Moreover, Leica TS06 total station with millimeter accuracy was employed to validate the measurements and the targets' position. Moreover, the SAR trajectory for each scenario is provided in Fig. 10-b. The sensor is fixed during the MIMO radar data acquisition. In GBSAR data acquisition mode to estimate detected targets' linear displacement, the radar sensor repeatedly moves a distance of 8 cm with mean velocity of 22 mm/s. For the case of vibration monitoring, linear SAR trajectory with the mean velocity of 25 mm/s was considered.

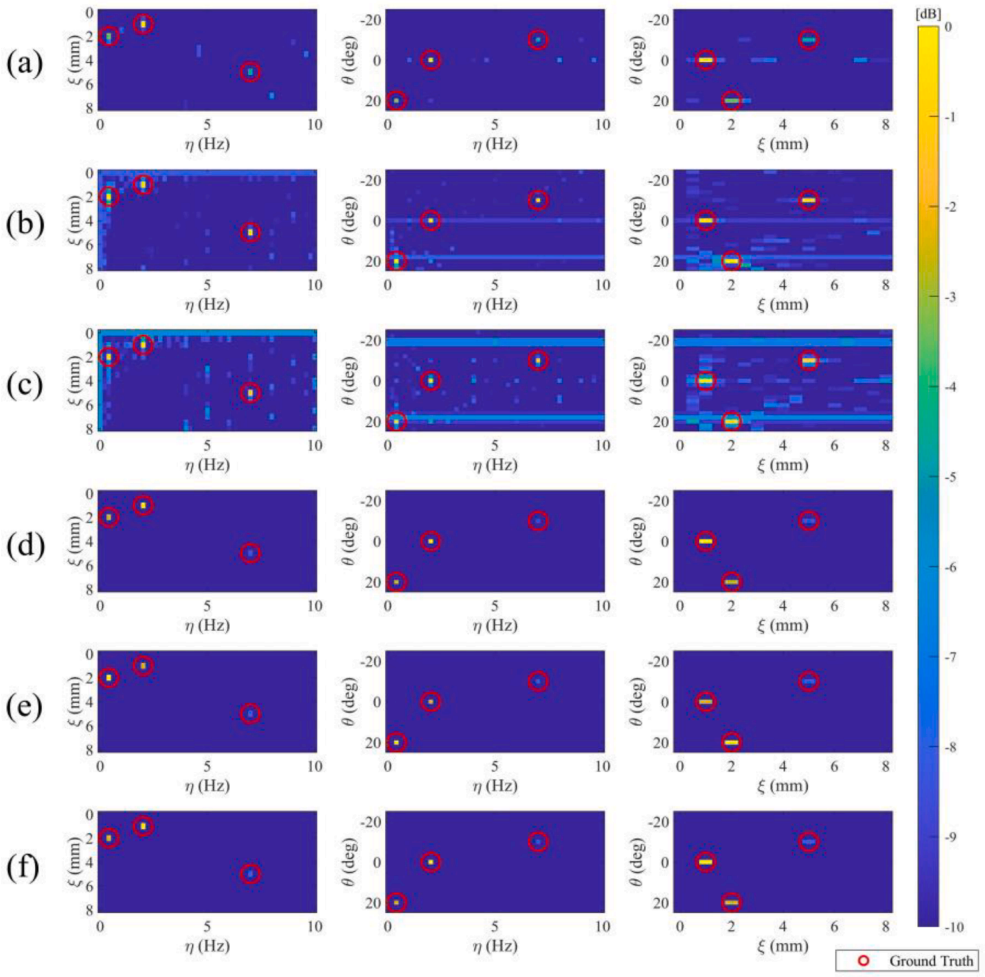

Fig. 9. Power spectrum densities for vibrational displacement monitoring for different SAR trajectories by Capon estimator: a) Random trajectory, b) Linear trajectory, c) Zigzag trajectory after CLEAN algorithm, d) Random trajectory after CLEAN algorithm, e) Linear trajectory after CLEAN algorithm, f) Zigzag trajectory after CLEAN algorithm.

Table 5
Applicability of the investigated SAR trajectories for sub-second linear and vibrational displacement monitoring.

Monitoring scenario	Random (physically not possible)	Linear	Zigzag (continuous repeat-pass)
Linear Velocity	✓	×	✓
Vibration	✓	✓	✓

Similar to the simulated results, four experiments were carried out by processing the MIMO radar and GBSAR signals. Table 6 summarizes the parameters of the experimented scenarios. The moving target is located at the 5.6 m slant distance from the imaging system, where in the linear displacement scenario, the target moves toward the sensor's LOS direction with velocity $v = 5$ mm/s, and in the case of the vibration displacement scenario, the target vibrates with 5 mm amplitude and 0.2 Hz frequency. The data acquisition interval was set to be 0.02 s in all experiments, which indicates the repetition time for each range-azimuth data acquisition in MIMO radar and range profile acquisition in GBSAR modes.

After implementing the proposed method on every range bin corresponding to the monitoring area, the detected points were superimposed on the optical orthophoto of the scene. Accordingly, Fig. 11 and Fig. 12 show the detected targets' linear displacement velocity and vibration characteristics (amplitude and frequency), respectively. While the detected points distribution looks almost similar in the implemented SE methods, the low-resolution experiments with short synthetic aperture length of MIMO radar have provided a wider range of points around the scattering targets. However, experiments by GBSAR signal, because of longer synthetic aperture length and better cross-range resolution, detected a lower number of scattering points around each CR. By the way, the estimated displacement parameters for fixed and moving targets are close to the reference values, and in all cases, the targets'

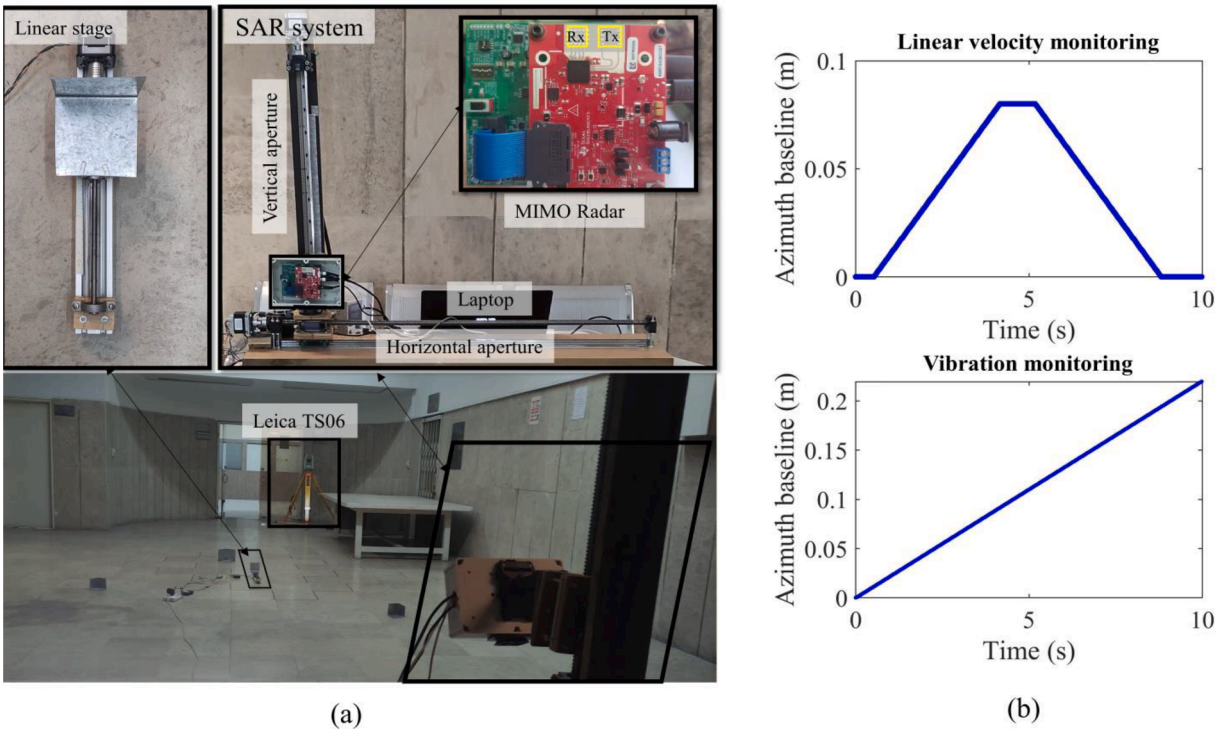

Fig. 10. Experimental setup: a) used instruments, including MIMO radar, GBSAR, fixed and moving corner reflectors, and Leica TS06 total station, b) defined SAR trajectories for velocity and vibration monitoring scenarios.

Table 6
Data acquisition characteristics of the real experiments.

Monitoring Scenario	Imaging mode	Aperture length (mm)	Signal acquisition interval (s)*	Total time of Acquisition (s)	Targets' characteristics**
Linear velocity	MIMO	15.2	0.02	10	r = [5.6]
	SAR	80	0.02	10	θ = [-3]
					v = [-0.5]
Vibration	MIMO	15.2	0.02	10	r = [5.6]
	SAR	250	0.02	10	θ = [-3]
					ξ = [5]
					η = [0.2]

* Here, the definition of "signal acquisition interval" for MIMO radar imaging is the repetition time for acquiring full range-azimuth data, and for the GBSAR imaging is the repetition time for the acquisition of each range signal.

** r denotes simulated targets' range in m, θ denotes targets' azimuth angle in deg, v is the targets' linear velocity in cm/s, ξ denotes vibration amplitude of targets in mm, and η denotes vibration frequency of targets in Hz.

localization look accurate.

The quantitative results of real experiments are presented in Table 7. The estimation and target focusing capabilities of each scenario and estimator were evaluated using SNR and PSLR metrics, while the targets' AoA localizations were evaluated by the observed angle from the Leica TS06 total station, which provides 5″ angular accuracy (about 0.001°). The use of SE methods considerably improved the capability to estimate displacement parameters compared to the conventional FT estimator. SAR demonstrated similar results to MIMO imaging mode, while its longer aperture length resulted in better angular resolution. However, the main reason for the lower SNR and PSLR of SAR imaging mode could be due to the unideal trajectory during data acquisition. More specifically, in the case of AoA-velocity estimation, as shown in Fig. 13, Capon and MUSIC performed better than BF, with better background suppression. Also, the quantitative results showed higher SNR and PSLR for these estimators. As shown, the undesired effects of SAR trajectory seem to be more present in the obtained image by BF, while Capon shows promising capability in suppressing these signals. In fact, these cross-like sidelobes are due to the uniform sampling of the radar's azimuth track, as discussed in the previous section, which seems inevitable in practical problems for real-time displacement monitoring.

Regarding the accurate localization of targets, the angular error by processing MIMO radar varied between 1.46°−3.61° degrees. In comparison, due to the longer synthetic aperture length, and consequently better angular discriminability, the results of SAR imaging improved the target localization in the range of 0.92°−1.40°. Similar to the simulated experiments, we set $\omega = 0.9$ and 5 iterations of

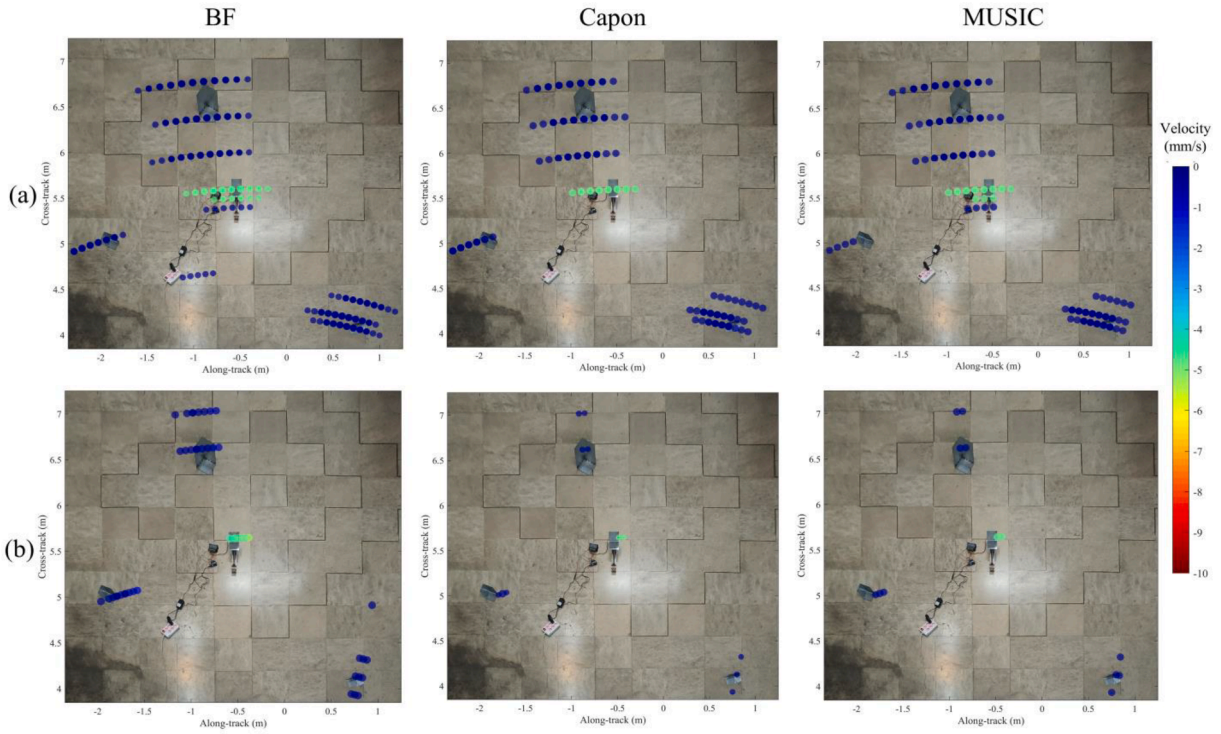

Fig. 11. Detected points in azimuth-velocity space by SE methods, superimposed on the optical orthophoto: a) MIMO, b) GBSAR (colormap denotes velocity and points' size denotes relative backscattering power).

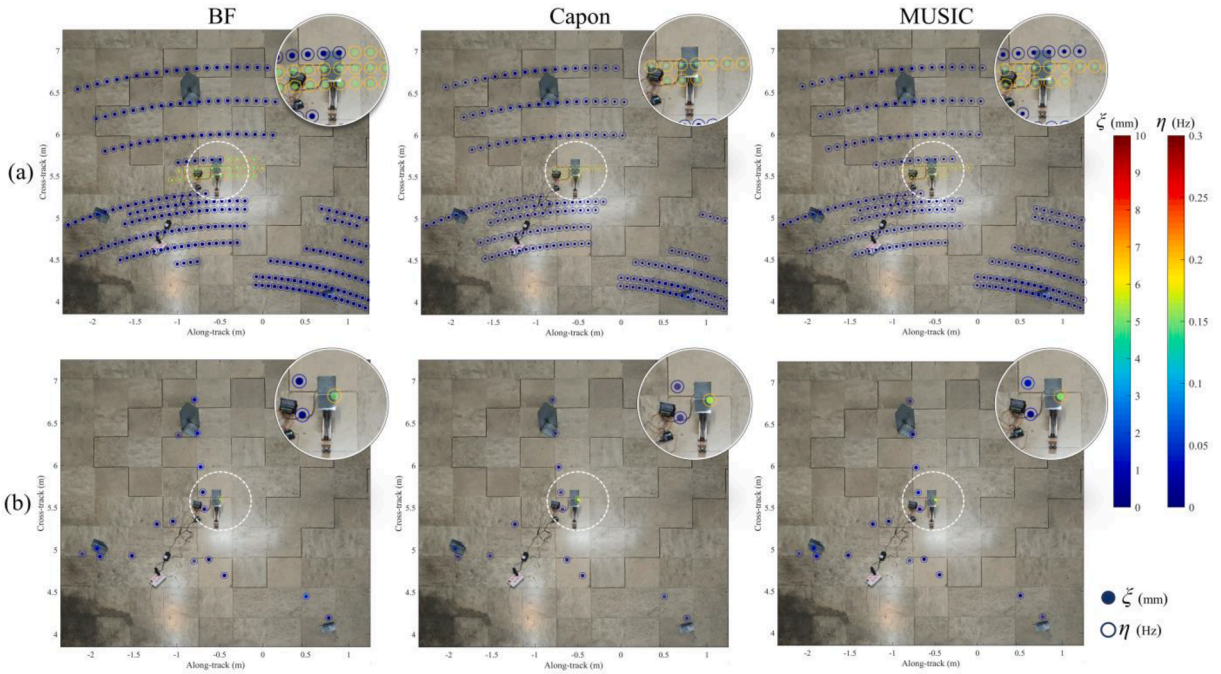

Fig. 12. Detected points in azimuth-vibration space by SE methods, superimposed on the optical orthophoto: a) MIMO, b) GBSAR (colormaps denote vibration amplitude and frequency and points' size denotes relative backscattering power.).

Table 7
Evaluation results of real experiments (Numbers are in dB).

Estimator	Metric	Linear velocity monitoring				Vibration monitoring			
		MIMO		SAR		MIMO		SAR	
			CLEAN		CLEAN		CLEAN		CLEAN
BF	SNR	21.12	27.94	17.39	24.65	18.98	24.66	14.95	18.17
	PSLR	14.17	20.50	5.36	12.49	3.69	10.00	3.28	5.53
	AoA RMSE	3.42	0.34	1.25	1.54	3.61	0.52	1.40	0.94
Capon	SNR	27.27	31.93	25.49	32.15	23.07	29.96	17.64	24.53
	PSLR	20.67	28.44	10.97	19.05	7.64	18.24	7.45	12.76
	AoA RMSE	1.46	0.62	1.04	1.22	2.38	0.52	0.92	0.82
MUSIC	SNR	25.60	33.19	20.62	28.50	22.50	29.59	17.11	26.05
	PSLR	16.15	23.74	8.24	16.12	6.90	14.32	5.23	12.37
	AoA RMSE	2.09	0.30	1.03	1.54	2.94	0.52	1.07	1.01
FT	SNR	5.1	–	–	–	–	–	–	–
	PSLR	10.16	–	–	–	–	–	–	–
	AoA RMSE	5.17	–	–	–	–	–	–	–

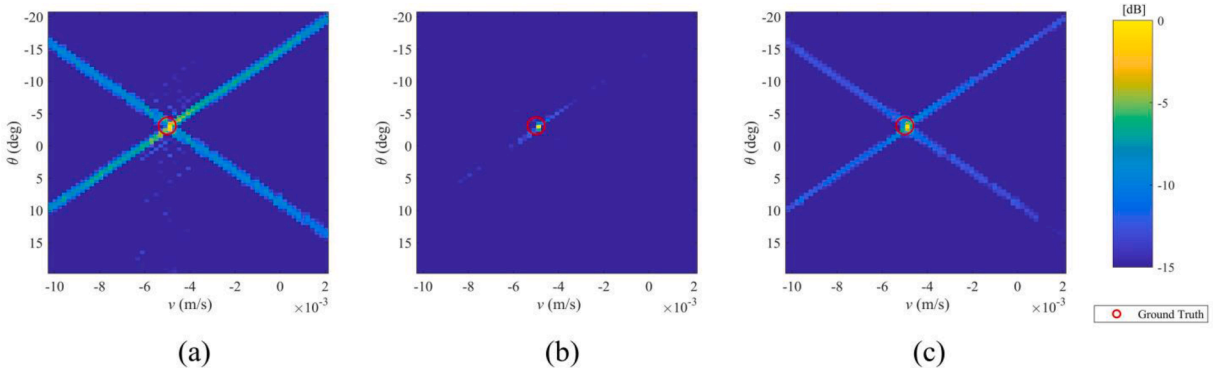

Fig. 13. Estimated power spectrum densities for azimuth angle of arrival and velocity retrieval in real experiments based on a) Beamforming, b) Capon, c) MUSIC.

CLEAN algorithm. However, after performing the CLEAN algorithm on the initially estimated PSDs, along with significant improvement in SNR and PSLR in each scenario, it can be noticed that the angular error by MIMO imaging was significantly improved up to 0.3°. This improvement was weaker for SAR imaging scenarios because, in contrast to MIMO, which provides wide signals due to its low resolution, SAR provides sharp and narrow peak signals even without performing CLEAN. In fact, the effect of CLEAN algorithm on MIMO imaging is both suppressing the background and interferences, as well as narrowing the peak signals. However, SAR already provides narrow peak signals in the location of targets due to the high angular resolution. Thus, the only significant effect of CLEAN on SAR imaging would be improving the SNR by suppressing the background and trajectory traces, and improving the targets' PSLR by reducing the effects of interferences. The effect of CLEAN is also shown in Fig. 14 and Fig. 15 for velocity and vibration estimation scenarios, respectively. As can be observed, in SAR imaging mode the effect of trajectory is significantly reduced, while the effect on narrowing the peak signal of target is negligible. However, the results by MIMO imaging show background suppression as well as

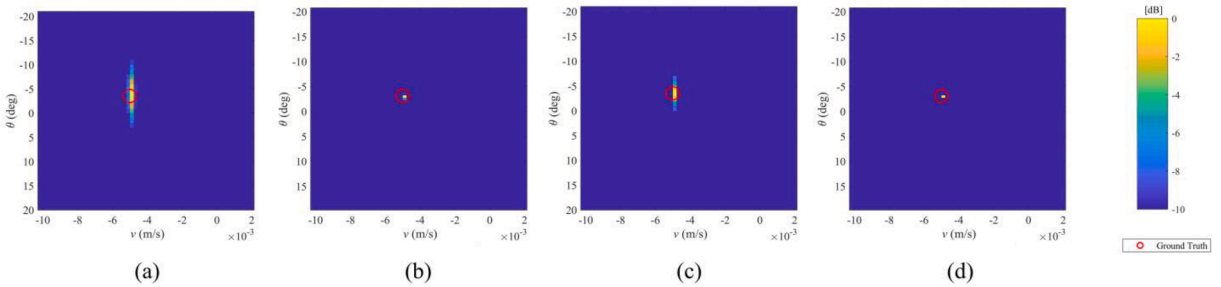

Fig. 14. Comparison of imaging modes' azimuth and velocity retrieval by Capon estimator: a) MIMO, b) SAR, c) MIMO after CLEAN algorithm, d) SAR after CLEAN algorithm.

narrowing the target's impulse response.

In particular, it can be noticed that in the case of velocity estimation by SAR data, the angular error was slightly increased after performing CLEAN, and in a similar situation, MIMO radar's angular error is lower. This could be due to the reason that during MIMO imaging, the sensor remains intact, and thus, the sensor's localization error and errors caused by movement of the sensor are at a minimum. However, during SAR imaging mode, the sensor is moving on a back-and-forth trajectory during the data acquisition, which is prone to sensor localization and mechanical errors. Overall, according to the results, the angular error for SAR imaging mode based on the presented method is less than 1.54°, and for the MIMO imaging, the angular error reduces up to 0.3°, which is promising. Furthermore, in most cases, the estimated PSDs possess SNR higher than 25 dB, and the targets are focused with PSLRs higher than 15 dB, which indicates the strong capability of the proposed methods for background suppression and highlighting scattering targets, respectively.

4. Conclusion

This paper proposed a multi-dimensional monitoring system based on SE methods to estimate fast sub-second displacements of targets using ground-based radar signals. Acquiring a single track of data from GBSAR systems typically takes several minutes. As a result, existing methods primarily focus on monitoring slow displacements with GBSAR systems and overlook possible displacements during the data acquisition process. To address this issue, MIMO radars were employed. However, the cross-range resolution of MIMO radar is limited by the number and geometry of physical transmitter and receiver antennas. Additionally, antenna array interference and the presence of multiple scatterers can affect data quality, resulting in sidelobes and grating lobes. This paper presented a workflow to overcome the limitations of high-resolution and real-time linear and vibrational displacement monitoring using GBSAR and MIMO radar data. The theoretical aspects of signal models for estimating azimuth AoA, linear displacement velocity, and vibrations, along with the corresponding processing steps, were provided and discussed for both MIMO and GBSAR data acquisition modes.

Various experiments based on numerical simulations and real data were conducted. The signals were collected from our developed GBSAR system, which utilizes the TI-AWR1642 radar sensor with MIMO imaging capability and millisecond acquisition interval. The proposed method was implemented using BF, Capon, and MUSIC estimators. Additionally, the CLEAN algorithm was adapted to suppress the effects of background and sidelobes in the estimated PSD, resulting in clear peak signals at the targets' locations. The results demonstrate that the proposed methods can effectively be applied to MIMO radar imaging with high data repetition, exhibiting lower sidelobe levels compared to the prevalent FT algorithm and higher SNR. The proposed method was successfully implemented on

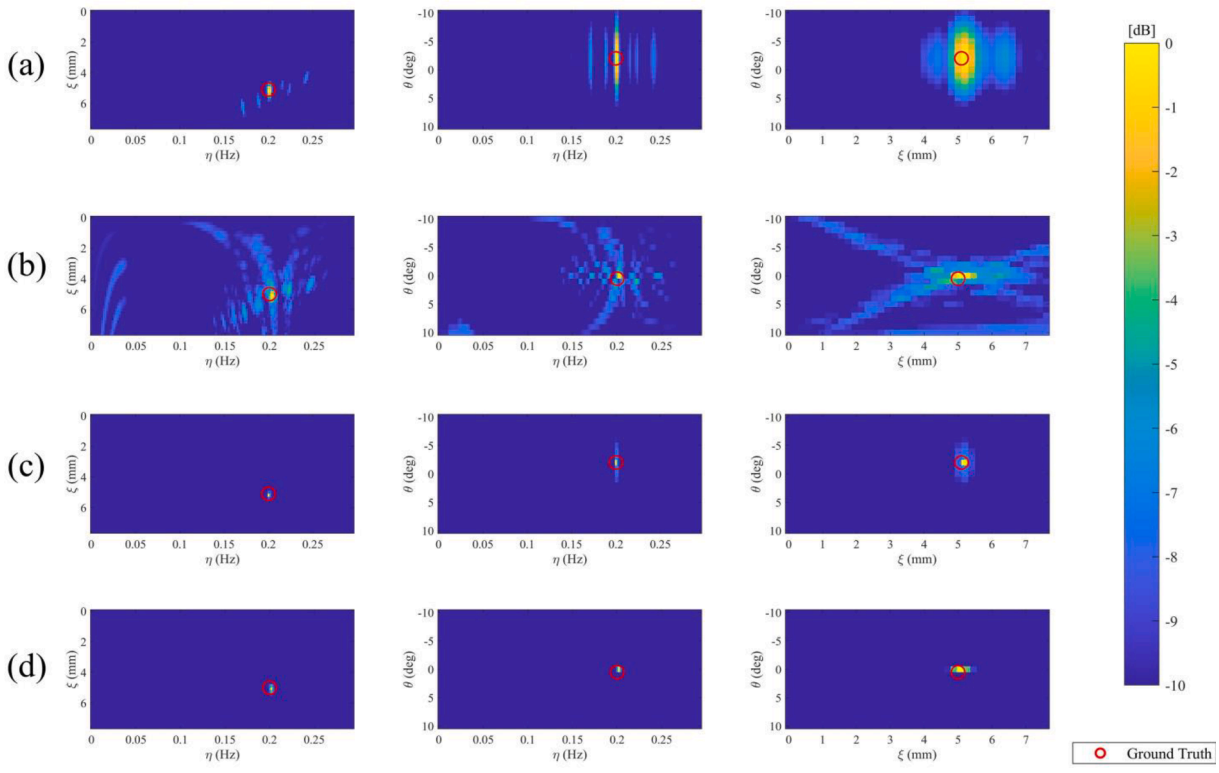

Fig. 15. Comparison of imaging modes' azimuth and vibration retrieval from real experiments by Capon estimator: a) MIMO, b) SAR, c) MIMO after CLEAN algorithm, d) SAR after CLEAN algorithm.

GBSAR signals, yielding results with SNR and PSLR close to those of MIMO radar data. Moreover, the cross-range discriminability was significantly improved due to the longer synthetic aperture length and the proposed workflow. Various analyses were conducted to assess the robustness of the methods, including the effect of noise level, interference of multiple scatterers in one range bin, and SAR length and trajectory. The implemented SE methods exhibited similar performance in most cases, with the Capon method slightly outperforming the others.

Future work can be dedicated to applying and evaluating the performance of the presented workflow on different case studies of structural monitoring with ground-based radars, such as bridges, towers, and pipelines. Another interesting topic would be to extend and evaluate this method by using multiple concurrent sensors with different viewing angles.

Declaration of Competing Interest

The authors declare that they have no known competing financial interests or personal relationships that could have appeared to influence the work reported in this paper.

Data availability

Data will be made available on request.

References

[1] R. Bamler, P. Hartl, Synthetic aperture radar interferometry, Inverse Prob. 14 (1998) R1.
[2] A. Pepe, F. Calò, A Review of Interferometric Synthetic Aperture RADAR (InSAR) Multi-Track Approaches for the Retrieval of Earth's Surface Displacements, Applied Sciences 2017, Vol. 7, Page 1264. 7 (2017) 1264. https://doi.org/10.3390/APP7121264.
[3] A. Radman, M. Akhoondzadeh, B. Hosseiny, Integrating InSAR and deep-learning for modeling and predicting subsidence over the adjacent area of Lake Urmia, Iran, Gisci. Remote Sens. 58 (2021) 1413–1433.
[4] A. Reigber, R. Scheiber, M. Jager, P. Prats-Iraola, I. Hajnsek, T. Jagdhuber, K.P. Papathanassiou, M. Nannini, E. Aguilera, S. Baumgartner, R. Horn, A. Nottensteiner, A. Moreira, Very-High-Resolution Airborne Synthetic Aperture Radar Imaging: Signal Processing and Applications, Proceedings of the IEEE. 101 (2013) 759–783. https://doi.org/10.1109/JPROC.2012.2220511.
[5] W. Li, Z. Wang, Y. Wang, J. Wu, J. Wang, Y. Jia, G. Gui, Classification of high-spatial-resolution remote sensing scenes method using transfer learning and deep convolutional neural network, IEEE J. Sel. Top. Appl. Earth Obs. Remote Sens. 13 (2020) 1986–1995.
[6] G. Zhang, Y. Wu, W. Zhao, J. Zhang, Radar-based multipoint displacement measurements of a 1200-m-long suspension bridge, ISPRS J. Photogramm. Remote Sens. 167 (2020) 71–84.
[7] V. Akbari, T.R. Lauknes, L. Rouyet, J. Negrel, T. Eltoft, Validation of SAR iceberg detection with ground-based radar and GPS measurements, International Geoscience and Remote Sensing Symposium (IGARSS). 2018-July (2018) 4623–4626. https://doi.org/10.1109/IGARSS.2018.8517286.
[8] O. Monserrat, M. Crosetto, G. Luzi, A review of ground-based SAR interferometry for deformation measurement, ISPRS J. Photogramm. Remote Sens. 93 (2014) 40–48.
[9] M. Pieraccini, L. Miccinesi, Ground-based radar interferometry: A bibliographic review, Remote Sens. (Basel) 11 (2019) 1029.
[10] B. Hosseiny, J. Amini, S. Safavi-Naeini, Simulation and Evaluation of an mm-Wave MIMO Ground-Based SAR Imaging System for Displacement Monitoring, in: 2021 IEEE International Geoscience and Remote Sensing Symposium IGARSS, IEEE, 2021: pp. 8213–8216. Doi: 10.1109/IGARSS47720.2021.9553347.
[11] J. Broussolle, V. Kyovtorov, M. Basso, G.F.D.S.E. Castiglione, J.F. Morgado, R. Giuliani, F. Oliveri, P.F. Sammartino, D. Tarchi, MELISSA, a new class of ground based InSAR system. An example of application in support to the Costa Concordia emergency, ISPRS J. Photogramm. Remote Sens. 91 (2014) 50–58.
[12] F. Mugnai, D. Tarchi, Multiple-input multiple-output radar, ground-based MIMO SAR for ground deformation monitoring, Europ. J. Remote Sens. 55 (2022) 604–621.
[13] A. Baumann-Ouyang, J.A. Butt, D. Salido-Monzú, A. Wieser, MIMO-SAR Interferometric Measurements for Structural Monitoring: Accuracy and Limitations, Remote Sensing 2021, Vol. 13, Page 4290. 13 (2021) 4290. https://doi.org/10.3390/RS13214290.
[14] G. Ciattaglia, A. De Santis, D. Disha, S. Spinsante, P. Castellini, E. Gambi, Performance Evaluation of Vibrational Measurements through mmWave Automotive Radars, Remote Sensing 2021, Vol. 13, Page 98. 13 (2020) 98. https://doi.org/10.3390/RS13010098.
[15] B. Hosseiny, J. Amini, H. Aghababaei, Interferometric Processing of a Developed Mimo Gbsar for Displacement Monitoring, ISPRS Annals of the Photogrammetry, Remote Sensing and Spatial Information Sciences. X-4/W1-202 (2023) 301–306. https://doi.org/10.5194/isprs-annals-x-4-w1-2022-301-2023.
[16] L. Miccinesi, T. Consumi, A. Beni, M. Pieraccini, W-band MIMO GB-SAR for Bridge Testing/Monitoring, Electronics 10 (2021) 2261.
[17] A.M. Guarnieri, J. Wang, Y. Wang, Y. Li, X. Huang, Fast Displacement Estimation of Multiple Close Targets with MIMO Radar and MUSICAPES Method, Remote Sensing 2022, Vol. 14, Page 2005. 14 (2022) 2005. https://doi.org/10.3390/RS14092005.
[18] A. Baumann-Ouyang, J.A. Butt, M. Varga, A. Wieser, MIMO-SAR Interferometric Measurements for Wind Turbine Tower Deformation Monitoring, Energies 16 (2023) 1518.
[19] G. Fornaro, F. Lombardini, A. Pauciullo, D. Reale, F. Viviani, Tomographic processing of interferometric SAR data: Developments, applications, and future research perspectives, IEEE Signal Process Mag. 31 (2014) 41–50.
[20] H. Aghababaei, G. Ferraioli, L. Ferro-Famil, Y. Huang, M.M. d'Alessandro, V. Pascazio, G. Schirinzi, S. Tebaldini, Forest SAR tomography: Principles and applications, IEEE Geosci. Remote Sens. Mag. 8 (2020) 30–45.
[21] C. Rambour, A. Budillon, A.C. Johnsy, L. Denis, F. Tupin, G. Schirinzi, From interferometric to tomographic SAR: A review of synthetic aperture radar tomography-processing techniques for scatterer unmixing in urban areas, IEEE Geosci. Remote Sens. Mag. 8 (2020) 6–29.
[22] M. Crosetto, O. Monserrat, M. Cuevas-González, N. Devanthéry, B. Crippa, Persistent Scatterer Interferometry: A review, ISPRS J. Photogramm. Remote Sens. 115 (2016) 78–89, https://doi.org/10.1016/j.isprsjprs.2015.10.011.
[23] F. Xue, X. Lv, F. Dou, Y. Yun, A review of time-series interferometric SAR techniques: A tutorial for surface deformation analysis, IEEE Geosci. Remote Sens. Mag. 8 (2020) 22–42.
[24] Z. Wang, Z. Li, J. Mills, A new approach to selecting coherent pixels for ground-based SAR deformation monitoring, ISPRS J. Photogramm. Remote Sens. 144 (2018) 412–422.
[25] F. Lombardini, Differential tomography: A new framework for SAR interferometry, IEEE Trans. Geosci. Remote Sens. 43 (2005) 37–44.
[26] H. Aghababaee, G. Ferraioli, G. Schirinzi, V. Pascazio, Regularization of SAR tomography for 3-D height reconstruction in urban areas, IEEE J. Sel. Top. Appl. Earth Obs. Remote Sens. 12 (2019) 648–659.
[27] M. Schmitt, M. Shahzad, X.X. Zhu, Reconstruction of individual trees from multi-aspect TomoSAR data, Remote Sens. Environ. 165 (2015) 175–185.
[28] F. Banda, J. Dall, S. Tebaldini, Single and multipolarimetric P-band SAR tomography of subsurface ice structure, IEEE Trans. Geosci. Remote Sens. 54 (2015) 2832–2845.

[29] G. Fornaro, S. Verde, D. Reale, A. Pauciullo, CAESAR: An approach based on covariance matrix decomposition to improve multibaseline–multitemporal interferometric SAR processing, IEEE Trans. Geosci. Remote Sens. 53 (2014) 2050–2065.
[30] H. Aghababaei, On the assessment of non-local multi-looking in detection of persistent scatterers using SAR tomography, Remote Sens. (Basel) 12 (2020) 3195.
[31] S. Li, Y. Xiong, X. Shen, Z. Peng, Multi-scale and full-field vibration measurement via millimetre-wave sensing, Mech. Syst. Sig. Process. 177 (2022), 109178.
[32] Z. Ren, Y. Xiong, Z. Peng, G. Meng, 3D microwave vibrometer: Contactless three-dimensional vibration measurements using microwave radars, Mech. Syst. Sig. Process. 183 (2023), 109622.
[33] B. Hosseiny, J. Amini, H. Aghababaei, Structural displacement monitoring using ground-based synthetic aperture radar, Int. J. Appl. Earth Obs. Geoinf. 116 (2023), 103144, https://doi.org/10.1016/j.jag.2022.103144.
[34] B. Hosseiny, J. Amini, N. Zahedi, Two dimensional Ground-based SAR for improving cross-range resolution for monitoring remote sensing objects, Earth Observat. Geomat. Eng. (2022). https://doi.org/10.22059/EOGE.2022.346252.1121.
[35] N. Rojhani, M. Passafiume, M. Lucarelli, G. Collodi, A. Cidronali, Assessment of Compressive Sensing 2 × 2 MIMO Antenna Design for Millimeter-Wave Radar Image Enhancement, Electronics 9 (2020) 624, https://doi.org/10.3390/electronics9040624.
[36] D. Tarchi, F. Oliveri, P.F. Sammartino, MIMO radar and ground-based SAR imaging systems: Equivalent approaches for remote sensing, IEEE Trans. Geosci. Remote Sens. 51 (2012) 425–435.
[37] C.-Y. Chen, Signal processing algorithms for MIMO radar, California Institute of Technology, 2009.
[38] M. Soumekh, Synthetic aperture radar signal processing, Wiley, New York, 1999.
[39] J. Fortuny-Guasch, A fast and accurate far-field pseudopolar format radar imaging algorithm, IEEE Trans. Geosci. Remote Sens. 47 (2009) 1187–1196.
[40] W. Zhang, G. Li, Z. Wang, H. Wu, Non-contact monitoring of human heartbeat signals using mm-wave frequency-modulated continuous-wave radar under low signal-to-noise ratio conditions, IET Radar Sonar Navig. 16 (2022) 456–469.
[41] M.A. Siddique, U. Wegmüller, I. Hajnsek, O. Frey, Single-look SAR tomography as an add-on to PSI for improved deformation analysis in urban areas, IEEE Trans. Geosci. Remote Sens. 54 (2016) 6119–6137.
[42] J. Capon, High-resolution frequency-wavenumber spectrum analysis, Proc. IEEE 57 (1969) 1408–1418.
[43] R. Schmidt, Multiple emitter location and signal parameter estimation, IEEE Trans. Antennas Propag. 34 (1986) 276–280.
[44] J. Högbom, Aperture synthesis with a non-regular distribution of interferometer baselines, Astronomy and Astrophysics Supplement, Vol. 15, p. 417. 15 (1974) 417.
[45] P. Sijtsma, CLEAN based on spatial source coherence, Int. J. Aeroacoust. 6 (2007) 357–374.
[46] D. Morata, D. Papamoschou, High-Resolution Continuous-Scan Beamforming, AIAA J. 61 (2023) 429–443.
[47] O.F. den Ouden, J.D. Assink, P.S. Smets, S. Shani-Kadmiel, G. Averbuch, L.G. Evers, CLEAN beamforming for the enhanced detection of multiple infrasonic sources, Geophys. J. Int. 221 (2020) 305–317.
[48] M. Gal, A. Reading, S. Ellingsen, K. Koper, R. Burlacu, S. Gibbons, Deconvolution enhanced direction of arrival estimation using one-and three-component seismic arrays applied to ocean induced microseisms, Geophys. J. Int. 206 (2016) 345–359.
[49] TI, AWR1642 data sheet, product information and support | TI.com, (n.d.). https://www.ti.com/product/AWR1642 (accessed May 19, 2022).
[50] Y. Wang, W. Hong, Y. Zhang, Y. Lin, Y. Li, Z. Bai, Q. Zhang, S. Lv, H. Liu, Y. Song, Ground-Based Differential Interferometry SAR: A Review, IEEE Geosci. Remote Sens. Mag. 8 (2020) 43–70.
[51] M.E. Yanik, D. Wang, M. Torlak, Development and Demonstration of MIMO-SAR mmWave Imaging Testbeds, IEEE Access 8 (2020) 126019–126038, https://doi.org/10.1109/ACCESS.2020.3007877.